The June 2026 Socorro swarm: A reactivation of rift-parallel normal faults above the Socorro Magma Body

Christopher M. Calvelage[1,*], Jessica R. Aerts[2], Susan L. Bilek[2], and Urbi Basu[2]

[1]EarthScope Consortium, Washington, D.C., USA
[2]New Mexico Institute of Mining and Technology, Socorro, New Mexico, USA

[*]**Corresponding author:** Christopher M. Calvelage, chris.calvelage@earthscope.org

ORCID

Christopher M. Calvelage	`https://orcid.org/0009-0005-9807-4255`
Jessica R. Aerts	`https://orcid.org/0009-0007-2819-8724`
Susan L. Bilek	`https://orcid.org/0000-0001-6291-237X`
Urbi Basu	`https://orcid.org/0000-0001-6786-1719`

Contents of this PDF: main text, pages 2–27; supplementary material, pages 28–33.

Non-peer reviewed **Research Article** submitted to SEISMICA

The June 2026 Socorro swarm: A reactivation of rift-parallel normal faults above the Socorro Magma Body

Christopher M. Calvelage * [1], **Jessica R. Aerts** [2], **Susan L. Bilek** [2], **Urbi Basu** [2]

[1]EarthScope Consortium, Washington, D.C., USA, [2]New Mexico Institute of Mining and Technology, Socorro, New Mexico, USA

Author contributions: *Conceptualization, Methodology, Software, Formal Analysis, Investigation, Data Curation, Visualization, Writing - Original draft*: Christopher M. Calvelage. *Resources, Data Curation, Writing - Review and Editing*: Jessica R. Aerts. *Resources, Data Curation, Writing - Review and Editing*: Susan L. Bilek. *Writing - Review and Editing*: Urbi Basu.

Abstract In June 2026 an earthquake swarm of maximum local magnitude (M_L) 3.9, comprising 425 matched-filter detections, occurred in the central Rio Grande rift about 45 km north of Socorro, New Mexico, above the northern margin of the Socorro Magma Body (SMB). This setting makes a magmatic or fluid origin the natural hypothesis. We test this hypothesis against the source physics, comparing the swarm with two decades of local seismicity. The swarm b-value is 0.51, low relative to a regional background near 0.83 that includes two prior swarms in the same region. Stress drops are about twice a regional baseline measured by the same method, with the largest events reaching about 10 MPa. The largest event has a well-resolved normal mechanism with no clear isotropic component, and the smaller events are weakly constrained but broadly consistent with normal faulting. Together, a low b-value, elevated stress drops, and the normal mechanisms place the swarm in the non-magmatic, high-differential-stress regime. We interpret the June 2026 swarm as a reactivation of multiple rift-parallel normal faults within the transverse San Acacia accommodation zone, influenced but not driven by the SMB.

Non-technical summary Earthquake swarms are bursts of many small earthquakes without a single dominant mainshock. They can be driven by underground fluids, by slow aseismic fault slip, or by ordinary tectonic stress, and telling these apart matters for earthquake hazard. In June 2026 a swarm of 425 earthquakes, the largest of magnitude 3.9, struck the Rio Grande rift north of Socorro, New Mexico, above the northern edge of a large body of partially molten rock in the middle crust. That setting makes a magma or fluid origin a natural first guess. We test it using the physics of the earthquake sources. Two measurements, the relative number of small to large events and the stress released by each rupture, together gauge stress and fluid content. The swarm has an unusually small proportion of small events, the signature of high stress, and its earthquakes released more stress per rupture than earlier earthquakes in the same area. Both, along with the

*Corresponding author: chris.calvelage@earthscope.org

style of faulting, point away from fluids and toward high tectonic stress. This swarm was under higher stress than two decades of earlier earthquakes in the same area, which is why it produced the largest event on record there. Although the swarm sat above a magma body, it was driven by tectonic stress, not by magma or fluids.

1 Introduction

Earthquake swarms are sequences of many events clustered in space and time without a single dominant mainshock. Their drivers fall into three broad classes, pressurized fluids or magma, aseismic slip, and ordinary tectonic loading, and distinguishing among them is a recurring problem in earthquake science (Danré et al., 2024; Shelly et al., 2016). Previous studies draw this distinction from signatures such as the migration pattern, the presence of deep long-period events, or the absence of a geodetic transient (Aki and Koyanagi, 1981; Lohman and McGuire, 2007; Roland and McGuire, 2009). Swarm events are complex and often contain dynamics attributable to fluids and ordinary mainshock-aftershock behavior.

Two source observables carry information about the stress state and the role of fluids. The first is the b-value of the frequency-magnitude distribution. Laboratory and field studies show that the b-value decreases with increasing differential stress, meaning a low b-value represents a highly stressed volume and a high b-value a weakly stressed volume (Scholz, 2015; Schorlemmer et al., 2005; Wu et al., 2018). Fluid injection and magmatic intrusion raise the b-value, and swarms beneath active volcanoes commonly show b-values near or above 1.2 (Farrell et al., 2009; Glazner and McNutt, 2021), although this elevation of the b-value is generally related to transient fluid pulses rather than a permanent property of volcanic settings (Roberts et al., 2015). A low b-value therefore argues against a fluid or magmatic driver and for high differential stress. Additionally, faulting style modulates b-values, with normal-faulting regimes tending toward higher values than thrust regimes (Schorlemmer et al., 2005). For the Socorro Magma Body region specifically, published estimates sit near the crustal values; Aerts and Bilek (2025) report 0.78 for the relocated 2002 to 2009 catalog, and Ruhl et al. (2010) found a rift-like b-value (0.9) for a 2009 microearthquake swarm above the body.

The second observable is the stress drop, the difference between the shear stress on the fault before and after rupture. Studies that control for faulting mechanism and depth find that the stress drops of fluid-induced and tectonic earthquakes overlap (Huang et al., 2017), and the global range for tectonic events spans more than two orders of magnitude (Allmann and Shearer, 2009). The absolute stress drop is therefore not diagnostic of the driving mechanism. What is informative is the stress drop of the swarm relative to a local baseline measured by the same method, which gauges how anomalous the swarm is within the surrounding region.

The June 2026 swarm occurred above the northern margin of the Socorro Magma Body (SMB). The sequence ran for nearly 6 days from 13 June to 19 June and produced 425 detected earthquakes, 210 of them on 14 June alone, well above the long-term regional average of about one earthquake per day. Ten events reached magnitude 3 or above and the largest reached M_L 3.9, exceeding anything in the modern record for the region. A sparse network records the 2026 swarm and its geometry only resolves a full moment tensor for the largest event and constrains the east-west hypocenter positions weakly. Because the b-value and the stress drop depend on the frequency-magnitude distribution and the source spectra rather than on azimuthal coverage or precise relative locations, they are insensitive to this limitation. We compare the 2026 swarm to a historical record containing two decades of regional seismicity to examine whether the sequence is fluid-driven or tectonic, and whether its source physics is anomalous for this region.

2 Tectonic and geophysical setting

The swarm lies in the central Rio Grande rift, one of the major Cenozoic continental rifts of North America, which extends from central Colorado into northern Mexico and accommodates roughly east-west crustal extension (Chapin and Cather, 1994). In its central segment near Socorro, the rift consists of a chain of north-trending axial basins bounded by north-striking normal faults (Chamberlin, 1982), superimposed on older Laramide compressional structures. Extension is slow, on the order of a millimeter per year across the rift region (Murray et al., 2019), and is taken up by these basin-bounding faults under a stress field with a near-vertical maximum compressive stress and an east-west minimum compressive stress (Heidbach et al., 2018).

The swarm occurred within the San Acacia accommodation zone (Grauch and Connell, 2013; Sion et al., 2020), a transverse structural belt that transfers extension between adjacent rift segments (Figure 1). Accommodation and transfer zones of this kind host faults and fabrics oblique to the dominant north-striking grain of the rift (Faulds and Varga, 1998; Minor et al., 2013; Sanford et al., 1995), inherited from older structures and from the geometry of segment linkage (Chapin and Cather, 1994; Heilman et al., 2019).

The 2026 swarm lies close to the northern boundary of the Socorro Magma Body (SMB), and its properties set the thermal and mechanical context for the region (Figure 1). Located in the mid-crust, the SMB is one of the larger known magma bodies in the continental United States. It was first identified from mid-crustal reflected phases that require a thin, sill-like zone of partial melt at about 19 km depth (Sanford et al., 1977), and mapping of those reflections shows that it extends over several thousand square kilometers (Balch et al., 1997; Rinehart et al., 1979). Repeated leveling and later interferometric measurements show ongoing surface uplift above the SMB at rates of a few millimeters per year, interpreted as slow inflation of the sill (Fialko and Simons, 2001). A Sentinel-1 line-of-sight velocity field for 2016 to 2025 from the OPERA surface-displacement product (NASA/JPL/OPERA, 2025) shows steady uplift of about 2 mm/yr centered on the mapped body (Figure 2). The melt warms the overlying crust and weakens the rock, and the regional velocity model carries a corresponding mid-crustal low-velocity zone at the depth of the sill (Balch et al., 1997; Nakai et al., 2017). The body is a long-lived, slowly inflating mid-crustal intrusion rather than an active eruptive system.

The SMB region has a documented history of seismic activity. A relocated catalog of seismicity above the SMB spanning 2002 to 2022 (Aerts, 2024), records thousands of small earthquakes organized into hundreds of spatial clusters, all of them shallower than the sill. The 2026 swarm occurred at the northern margin, where two smaller swarms occurred in 2004 and in 2012. The recurrence of swarms here over two decades establishes the accommodation zone as one that produces earthquakes, and the long local record provides the baseline against which we measure the 2026 source physics (Figure 1).

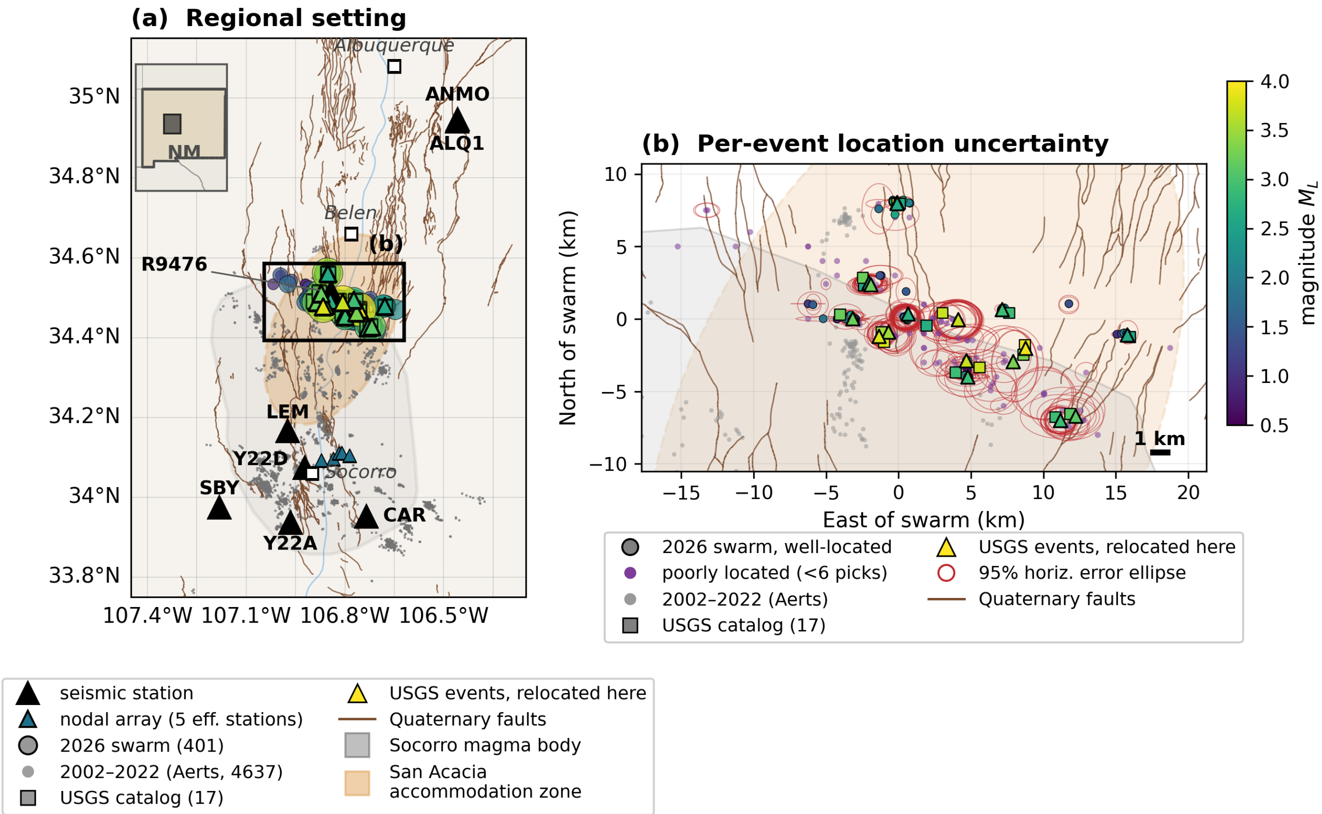

Figure 1 Regional and swarm-scale setting. (a) The 2026 swarm at the northern margin of the relocated historical seismicity of the SMB region, with Quaternary rift faults from the USGS Quaternary Fault and Fold Database (U.S. Geological Survey, 2020), the accommodation zone, and the stations. Black triangles are seismic stations and blue triangles the SmartSolo nodal array; the nearest station, AM.R9476, lies about 3 km north of the swarm. Squares are the USGS catalog hypocenters (U.S. Geological Survey, 2017) and the magnitude-colored triangles are our relocations of those same events. Small gray dots are the relocated 2002 to 2022 catalog of Aerts (2024). (b) Swarm-scale relocated hypocenters colored by local magnitude, with per-event horizontal location uncertainties from the GrowClust bootstrap drawn as 95 percent error ellipses (relative; median semi-axes about 730 m east and 390 m north, the east-west elongation reflecting the station distribution). Symbols follow panel (a). Events located from fewer than six correlated arrivals are shown in purple, and the 2002 to 2022 catalog again in gray.

3 Data and methods

3.1 Networks and data

We analyzed continuous data from 2026 June 13 at 12:00 UTC; the 425 detections reported below span 2026 June 13 at 14:01 to 2026 June 19 at 08:58 UTC, a period of nearly 6 days. The swarm was recorded by a sparse local and regional network (Table 1). The nearest station is a Raspberry Shake (R9476) about 3 km from the swarm centroid, which records a single vertical component; the remaining stations are three-component instruments. Additional coverage comes from the New Mexico Tech (SC) network, operated by the New Mexico Institute of Mining and Technology, stations ANMO (IU) and ALQ1 (GS) near Albuquerque about 62 km away, and regional broadband stations. Three stations of the Arizona Broadband Seismic Network in eastern Arizona (AE.HANNA, W18A, X18A) at 248 to 286 km and azimuths of 248 to 286 degrees fill the western azimuth that the local network does not sample. They supply first-motion polarities for all ten events of magnitude 3 and above, not only for the largest. No station to the east was operating during the sequence, so the eastern quadrant remains unsampled. A SmartSolo nodal array consisting of 16 instruments, deployed over the Socorro Magma Body about 44 km south of the swarm, recorded continuously

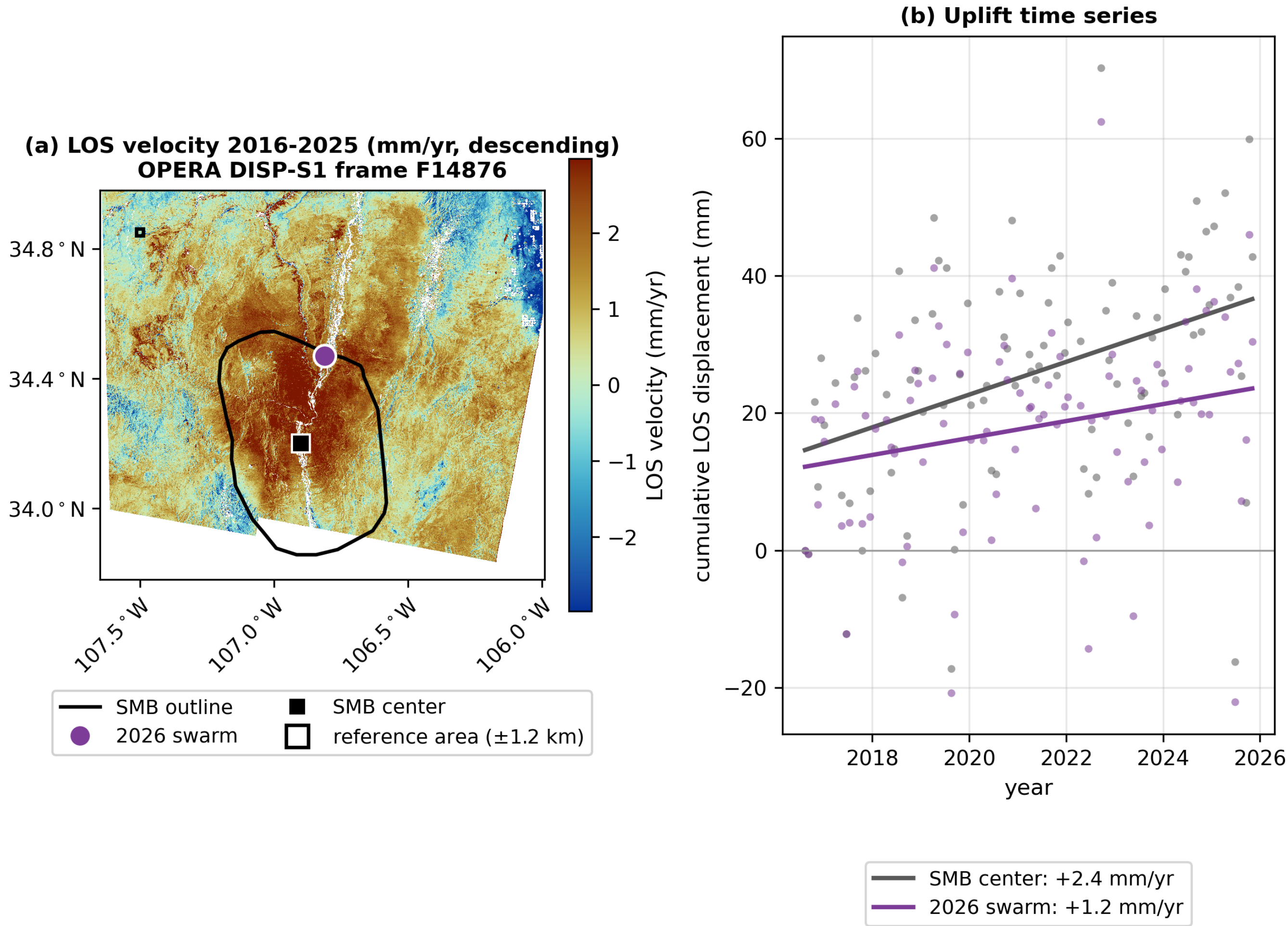

Figure 2 Persistent inflation of the SMB from Sentinel-1, 2016 to 2025 (OPERA surface- displacement product, descending track). (a) Line-of-sight velocity over the mapped SMB, referenced to a stable far-field area (open square, about 50 km north-west of the SMB), with the 2026 swarm on the northern flank. Coherent velocity covers the northern part of the SMB; the southern Rio Grande valley is too decorrelated to image, and the adjacent descending frame does not recover a usable signal there. (b) Monthly cumulative line-of-sight time series at the SMB center and at the swarm, each point a calendar-month median over an 18 km box, both showing steady uplift, about 2.4 mm/yr at the center and 1.2 mm/yr at the swarm (the velocity field in (a) gives about 2 mm/yr at the swarm). Positive line-of-sight is toward the satellite, consistent with uplift. The line-of-sight rate near the center corresponds to a vertical rate of about 3 mm/yr. A single descending track cannot separate vertical from horizontal motion, and the Sentinel-1 ascending gap that followed the 2021 sensor failure precludes a full ascending-plus-descending decomposition here.

through the sequence. Because the array lies at a southern azimuth already sampled by the SC stations, it densifies the source-parameter and relocation data but does not improve the azimuthal control needed for focal mechanisms. We therefore incorporate it as five effective stations, so that it does not over-weight that azimuth. The four easternmost nodes are used as individual stations. The remaining twelve occupy a single tight cluster 78 m across. Of these, only the six vertical-component nodes are used: we decimate their records from 1000 to 100 Hz and average them, into a single trace (NBEAM). The full recording geometry, including the array layout and the Arizona stations, is shown in Supplementary Figure S1. Telemetered waveforms and instrument metadata were obtained through EarthScope FDSN web services and the nodal data from the deployment archive.

3.2 Detection and relocation

We detected events by matched filtering with the ObsPy correlation detector, using 23 templates. Seventeen are USGS catalog events (U.S. Geological Survey, 2017). The remaining six come from a first detection pass made with those

Table 1 Principal stations used in this study. Distances and azimuths are measured from the swarm centroid. The SS entries are the SmartSolo nodal array about 44 km south.

Network	Station	Dist. (km)	Az. (deg)
AM	R9476	3	358
SC	LEM	38	199
SC	Y22D	47	189
SC	CAR	60	171
GS	ALQ1	61	35
IU	ANMO	62	35
SC	Y22A	62	191
SC	SBY	65	209
AE	HANNA	248	248
AE	W18A	274	286
AE	X18A	286	272
SS	56903	42	177
SS	53467	42	176
SS	54283	43	173
SS	52054	44	179
SS	NBEAM	44	184

17. We then ranked its detections by waveform similarity to the existing template set and kept the six best-recorded novel events. We reviewed and repicked them by hand, and promoted them to templates for a second pass. This targets the parts of the waveform space the catalog events do not span. For template j on channel i, the normalized cross-correlation with the continuous record d_i is

$$\mathrm{CC}_{ij}(t) = \frac{\sum_\tau d_i(t+\tau)\, s_{ij}(\tau)}{\sqrt{\sum_\tau d_i^2(t+\tau)}\,\sqrt{\sum_\tau s_{ij}^2(\tau)}}, \tag{1}$$

where s_{ij} is the template waveform. We declared a detection where the network-mean correlation $C_j(t) = N_{\mathrm{ch}}^{-1} \sum_i \mathrm{CC}_{ij}(t)$ exceeded a fixed threshold of 0.30, and we merged detections within a 6 s window so that a single earthquake is counted once across templates. Because the detector returns one correlation peak per template per earthquake, referenced to the template origin time rather than to an individual phase, P and S do not generate separate detections. This workflow yielded 425 detections, an increase of about 22 percent over the 349 detections of a catalog-only template set.

Matched-filter detections carry an origin time but no hypocenter, and GrowClust refines locations relative to a starting catalog rather than determining them from first arrivals, so we must first assign every detection an initial location. We assign initial locations as follows. The 17 catalog events started from the hypocenters published by the USGS and were passed through the same grid search as the other detections. For each detection we refined the P- and S-wave arrivals by cross-correlating its waveform against the matched template at each station, retained arrivals with correlation coefficient above 0.6, and searched a three-dimensional grid (horizontal ± 20 km, depth 2 to 20 km at 1 km spacing) for the hypocenter that minimizes the correlation-weighted root-mean-square of the differential travel-time residuals, with the event origin time solved analytically. Travel times were computed by the TauP method through the layered Nakai Socorro crustal model (Nakai et al., 2017), including its mid-crustal low-velocity zone. Detections with fewer than four correlated arrivals were left unlocated. This single-event grid search supplies the starting catalog that GrowClust then refines.

We relocated the detected events with the GrowClust algorithm (Trugman and Shearer, 2017; Trugman et al., 2023), a hybrid hierarchical-clustering and relative-relocation method that is less sensitive to velocity-model error and to outlier data than damped least-squares double difference. For event pairs i and j recorded at station k we formed the differential-time residual

$$dr_k^{ij} = \left(t_k^i - t_k^j\right)^{\text{obs}} - \left(t_k^i - t_k^j\right)^{\text{cal}}, \qquad (2)$$

measuring the observed differential times by waveform cross-correlation of the P and S arrivals on the vertical component and keeping pairs with correlation coefficient at least 0.7. GrowClust groups events into similarity clusters and relocates the members of each cluster relative to one another by an L1-robust shrinking-box search through the Nakai low-velocity-zone model, estimating the differential origin time of each pair internally. Of the 401 initially located events, the algorithm grouped 356 into multi-event clusters and relocated them relative to one another, leaving the ungrouped events at their starting positions. We estimated relative location uncertainties from a 100-sample bootstrap. The resampled distributions are strongly heavy-tailed, so we use the 95th percentile of the resample deviation rather than a median-deviation statistic, which would contain only half the resamples and understate the uncertainty. Using this metric, 95 percent of resamples fall within an area of about 730 m east, 390 m north and 860 m in depth, the corresponding median deviations are 103 m horizontally and 63 m vertically. The east-west uncertainty is about twice the north-south, which follows directly from the station distribution, and the absolute depth is less well resolved due to station coverage. The full distributions are given in Supplementary Figure S2. As an independent check we also relocated the catalog using damped least-squares double difference (Waldhauser and Ellsworth, 2000), which recovers the same structure (median horizontal difference 0.23 km, or 0.34 km in three dimensions, and the same trend), confirming that the geometry is robust to the relocation method.

3.3 Magnitudes and a consistent magnitude scale

We computed local magnitudes from peak band-passed (2 to 12 Hz) S-wave amplitudes. Because all events share nearly the same source region and distance range, we used a per-station offset with unit slope,

$$M_L = \underset{s}{\text{median}} \left[\log_{10} A_s + b_s \right], \qquad (3)$$

where A_s is the peak amplitude at station s. The station term b_s is a single constant per station, held fixed across the whole sequence, and was set so that the magnitudes of the 17 USGS catalog events match their network magnitudes in the median; stations with large residual scatter were excluded. Over those 17 events the residual against the network magnitude has a mean of -0.03 and a standard deviation of 0.18. Because the term is per station rather than per event, it is insensitive to site and path differences between stations.

The historical comparison requires the 2026 and historical magnitudes on a single scale. Since the two catalogs share no events, we calibrate the offset through events that each catalog shares with the national ANSS catalog (U.S.

Geological Survey, 2017), regressing

$$M_{\text{ANSS}} = 0.88\, M_{\text{Aerts}} + 0.64 \tag{4}$$

(10 matched events, correlation 0.70, slope standard error 0.32, mean offset 0.38 magnitude units). The slope is not distinguishable from unity, and the calibration events span only the upper part of the magnitude range used below, so we mapped the 2026 magnitudes onto the historical scale by subtracting the mean offset of 0.38, and used the regression, with its slope varied over two standard errors, as a sensitivity test. As reported below, the swarm b-value remains below the regional background across the entire range of uncertainty, so the comparison does not depend on the alignment of magnitude scales.

3.4 b-value

The frequency-magnitude distribution follows the Gutenberg-Richter relation

$$\log_{10} N(\geq M) = a - bM, \tag{5}$$

and we estimated b with the Aki-Utsu maximum-likelihood estimator (Aki, 1965),

$$\hat{b} = \frac{\log_{10} e}{\bar{M} - \left(M_c - \frac{1}{2}\Delta M\right)}, \tag{6}$$

where $\bar{M}$ is the mean magnitude above the completeness magnitude M_c and $\Delta M = 0.1$ is the magnitude bin width. This correction assumes magnitudes binned at ΔM; because our 2026 magnitudes are continuous and the historical catalog is reported to 0.01, we round every magnitude to the 0.1 bin before estimation and take M_c as the center of a bin. Its standard error follows Shi and Bolt (1982),

$$\sigma_b = 2.30\, b^2 \sqrt{\frac{\sum_i \left(M_i - \bar{M}\right)^2}{n\,(n-1)}}, \tag{7}$$

and we also report bootstrap confidence intervals, quoted throughout as the 16th to 84th percentiles of 2,000 resamples and equivalent to one standard error. We estimated M_c by the maximum-curvature method (Wiemer and Wyss, 2000), which takes the completeness magnitude as the bin that maximizes the non-cumulative frequency-magnitude distribution,

$$M_c = \arg\max_{M}\, n(M), \tag{8}$$

where $n(M)$ is the number of events in the magnitude bin of width ΔM centered on M. In every population here $\hat{b}$ rises steadily with the chosen M_c, well above any plausible completeness threshold. We therefore compared all populations at a common M_c on the aligned magnitude scale rather than at each catalog's own M_c. The maximum-curvature estimates range from 0.2 for the 2012 swarm to 0.6 for the 2026 swarm, with 0.5 for the full historical region, and we adopted $M_c = 0.4$ as the common value. This choice is conservative, since raising M_c increases the historical b-values more rapidly than that of the swarm. Evaluating each population at the swarm's own M_c of 0.6 yields a b-value of 0.57 for the swarm and 0.96 for the region, a larger separation than at the adopted value. Because a common M_c

does not equalize the magnitude range above the threshold, which also biases $\hat{b}$, we additionally refit each population using a doubly-truncated maximum-likelihood estimator (Page, 1968). Over a window shared by all four populations the swarm yields a b-value of 0.32 compared to 0.59 to 0.73 for the other three, a wider separation than at the common M_c (Supplementary Figure S3).

As a check insensitive to both M_c and a constant magnitude offset, we computed the b-positive estimator (van der Elst, 2021) from the differences of successive magnitudes, $\delta_i = m_{i+1} - m_i$. Positive differences $\delta_i \geq \delta_{\min}$ retain the Gutenberg-Richter slope while being unaffected by short-term incompleteness, and

$$\hat{b}^+ = \frac{\log_{10} e}{\langle \delta^+ \rangle - \delta_{\min} + \frac{1}{2}\Delta M}, \tag{9}$$

with $\delta_{\min} = \Delta M$. We then tested the cross-swarm result three ways. First, because b varies with depth, we recomputed the regional background using only historical events in the 7 to 13 km band that contains the swarm, so that the two populations are compared over the same depth range. Second, because a background dominated by clustered aftershock-like sequences can bias b, we split the historical catalog using its own cluster assignments and computed b separately for the declustered background and for the clustered events. Third, because the two catalogs are tied together by a regression rather than by shared events, we repeated the comparison across the full two-sigma range of the alignment slope, re-solving the intercept through the centroid of the calibration events at each slope, and also under the b-positive estimator, which is insensitive to a constant magnitude offset.

3.5 Stress drops

We estimated stress drops from displacement amplitude spectra of the direct S wave on the vertical component after instrument-response removal, where the SV arrival is well recorded at these takeoff angles. The nearest station, R9476 at 3 km, records only a vertical component, so we used the vertical throughout, measuring the swarm and the regional baseline on the same channel type. The P and S arrival times at each station were predicted through the Nakai velocity model from the event's hypocenter and depth, which matters at R9476, where the S wave of a 10 km deep event arrives 1 to 2 s later than an epicentral-distance estimate would place it. The signal window runs from 0.5 s before to 2.2 s after the S arrival and the noise window from 6 to 1 s before P. Records were demeaned, detrended, resampled to 100 Hz and high-passed at 1 Hz. Thirteen stations were used for the swarm, the eight permanent stations, the four individual nodes, and NBEAM. We took the seismic moment from the local magnitude through

$$\log_{10} M_0 = 1.5\, M_L + 9.1, \tag{10}$$

with M_0 in N m. This relation is defined for moment magnitude, so treating M_L as its equivalent introduces a systematic error wherever the two scales diverge, as they commonly do at small magnitudes. Because we apply the identical conversion to the swarm and to the regional baseline and report only the ratio of the two, this error is common to both populations and largely cancels. For each station we fit a joint model for an ω-squared source and a frequency-independent path attenuation,

$$A(f) = \frac{\Omega_0}{1 + (f/f_c)^2}\,\exp(-\pi f\,t^*), \tag{11}$$

over 2 to 22 Hz, where Ω_0 is the low-frequency level, f_c the source corner frequency, and t^* the path attenuation operator, and took the per-event corner frequency as the median over at least three stations. Windows whose standard deviation did not exceed 2.5 times that of the noise window were discarded, as were fits with the corner frequency within 0.2 Hz of the band edges, with t^* pinned at its bound of 0.15 s, or with a residual standard deviation above 0.5 in $\log_{10}$ amplitude. Events retaining fewer than three stations were dropped, in both the swarm and the regional baseline, because a two-station median is unstable given the station-to-station scatter in f_c. The stress drop of a circular source is

$$\Delta\sigma = \frac{7}{16}\,\frac{M_0}{r^3}, \qquad r = \frac{k\,\beta}{f_c}, \tag{12}$$

with source radius r, shear velocity $\beta = 3.5$ km/s, and $k = 0.37$ (Brune, 1970), so that $\Delta\sigma \propto M_0\,f_c^3$. We cross-checked corner frequencies by the empirical Green's function method on co-located high-correlation pairs, for which the spectral ratio

$$\frac{A_1(f)}{A_2(f)} = \frac{M_{0,1}}{M_{0,2}}\,\frac{1 + (f/f_{c,2})^2}{1 + (f/f_{c,1})^2} \tag{13}$$

cancels the shared path and site terms and isolates the two corner frequencies. Per-event uncertainty was taken as the interquartile range of the per-station estimates. Because the corner frequency must lie within the usable band, estimates below $M_L \approx 2.5$ are ignored, so we treat only $M_L \geq 2.5$ as reliable.

Because the stress drop scales as the cube of the corner frequency, the choice of k, β, and the spectral model propagates strongly into the absolute value (Abercrombie, 1995; Brune, 1970). For that reason, and because the absolute value is not directly diagnostic of the driving mechanism (Huang et al., 2017), we report the swarm stress drop as a ratio to a regional baseline computed by the same method.

3.6 Stress budget

We compared the differential stress that SMB inflation imposes at the swarm with the stress the swarm released. We modeled the SMB as a Mogi center of dilatation at 19 km depth, with the volume rate fixed by the observed surface uplift,

$$\frac{\mathrm{d}V}{\mathrm{d}t} = \frac{\pi d^2}{1-\nu}\,\dot{u}_z(0), \tag{14}$$

and evaluated the differential-stress rate at the swarm hypocenter,

$$\frac{\mathrm{d}(\sigma_1 - \sigma_3)}{\mathrm{d}t} = \frac{3\mu}{2\pi R^3}\,\frac{\mathrm{d}V}{\mathrm{d}t}, \tag{15}$$

where d is the source depth, $\dot{u}_z(0)$ the peak surface-uplift rate, R the source-to-swarm distance, and ν and μ the Poisson ratio and shear modulus. Accumulated over the inflation interval, this is the magmatic loading, which we compared with the per-event stress drop. The estimate is order-of-magnitude and is robust against factor-of-two changes in the uplift rate and the source depth; halving the source-to-swarm distance raises the loading eightfold, to about 0.7 MPa over 50 years, which still lies below the stress drop of the individual events.

3.7 Historical source physics

We compare the 2026 swarm against the relocated historical catalog of Aerts (2024), which spans 2002 to 2022 and contains 4,637 events assigned to 282 clusters. The published analysis of Aerts and Bilek (2025) covers the 2002 to 2009 portion of that catalog and its 17 primary clusters. The b-value comparison uses the aligned magnitude scale described above. Hypocenters, magnitudes, and depths for the 2026 events in every analysis below are taken from the GrowClust catalog. A stress-drop comparison at the level of the individual 2004 and 2012 swarms is not possible because those swarms contain no event above M_L 2. We instead established a regional baseline from the larger region-wide events, the 22 events of magnitude 2 and above with waveforms suitable for a corner-frequency fit at three or more stations, drawn from the part of the record from 2009 onward where such waveforms are available. For these we retrieved waveforms and responses from FDSN web services, restricting to vertical channels sampled at 50 Hz or higher within 120 km and taking every qualifying station in order of distance. These are mostly New Mexico Tech (SC) network stations, with IU.ANMO and GS, TA and X9 stations for the later events, at 8 to 114 km (123 station records over the 22 events), and we applied the identical preprocessing, windows, spectral fit and acceptance criteria through the same code. These 22 events lie 9 to 64 km from the 2026 swarm and are spatially distributed across the SMB region. Their stress drops increase with distance from the swarm and the regional station distances bracket the 2026 stations, which lie at 3 to 65 km.

3.8 Focal mechanisms

We computed a deviatoric regional moment tensor $\mathbf{M}$ for the largest event by waveform fitting with Computer Programs in Seismology (Herrmann, 2013) and an independent grid search, as a check on the USGS regional moment tensor (ANSS ComCat event us7000ssvm; U.S. Geological Survey 2017) that we adopt for this event. To bound a volumetric component, which a deviatoric inversion cannot resolve, we separately inverted the local first-motion polarities of the largest events for a full moment tensor with the Bayesian MTfit method (Pugh and White, 2018), decomposing each sample into isotropic and deviatoric parts,

$$\mathbf{M} = \tfrac{1}{3}\,\mathrm{tr}(\mathbf{M})\,\mathbf{I} + \mathbf{M}^{\mathrm{dev}}, \tag{16}$$

and report the isotropic term $\frac{1}{3}\mathrm{tr}(\mathbf{M})$ relative to the total moment, which is sensitive to any volumetric source. For events of magnitude 3 and above we used first-motion P polarities and S/P amplitude ratios (Hardebeck and Shearer, 2002; Skoumal et al., 2024); the polarity at station k is the sign of the far-field P radiation $\mathbf{u}_k^{\mathrm{T}}\mathbf{M}\,\mathbf{u}_k$, where $\mathbf{u}_k$ is the take-off direction. We added a custom grid search that incorporates the far western Arizona polarities the standard ray tracer does not reach at 250 to 290 km. To quantify what the three-azimuth geometry can resolve, we formed the matrix of P-radiation sensitivities $\partial(\mathbf{u}_k^{\mathrm{T}}\mathbf{M}\,\mathbf{u}_k)/\partial M_{ij}$ over the station set and examined its singular values; the small singular values identify the moment-tensor components the geometry cannot constrain, and we report mechanism uncertainties accordingly.

3.9 Migration and the diffusion test

We tracked the order and timing of the GrowClust families, distinguishing sequential along-strike activation, as a propagating front would produce, from episodic and out-of-order bursts. To test whether a diffusing pore-pressure front could account for the spatial spread, we compared the distance of each event from the nucleation against the triggering front $r = \sqrt{4\pi D t}$ (Shapiro et al., 1997), where D is the hydraulic diffusivity and t the time since onset, and we report the diffusivity the observed migration would require. Throughout, the nucleation and the swarm onset refer to the first detected event of the sequence, which is not the largest; the M_L 3.9 event occurred later.

4 Results

4.1 The 2026 swarm in two decades of context

The historical catalog shows swarms throughout the SMB region. It resolves the regional seismicity into 282 clusters, most of them small swarms of tens of events rather than mainshock-aftershock sequences. Two sequences elsewhere above the body have been characterized in detail, the October 2005 swarm (Stankova et al., 2008) and a 2009 microearthquake swarm (Ruhl et al., 2010), the latter attributed to failure of pre-existing fractured crust rather than to magma movement. Both show the same swarm-like character as the clusters nearer the 2026 sequence, and Stankova et al. (2008) further report reactivation of the same structures over decadal intervals. Two earlier swarms occurred in the same area, 53 events in 2004 and 38 in 2012, both below local magnitude about 2, against 425 detections (401 located) in 2026 (Figure 3b). For the b-value comparison below we use the calendar-year windows 2003 to 2005 (70 events, 53 above the common completeness magnitude) and 2011 to 2013 (44 events, 25 above), which include the lower-rate activity around each burst. The 2026 maximum M_L of 3.9 exceeds the entire modern record for the region; over the 2002 to 2022 span of the relocated catalog the largest event reached only magnitude 2.9. Once the two magnitude scales are aligned, that single 2026 event released a moment comparable to the cumulative moment of all 4,637 historical events (Figure 3a).

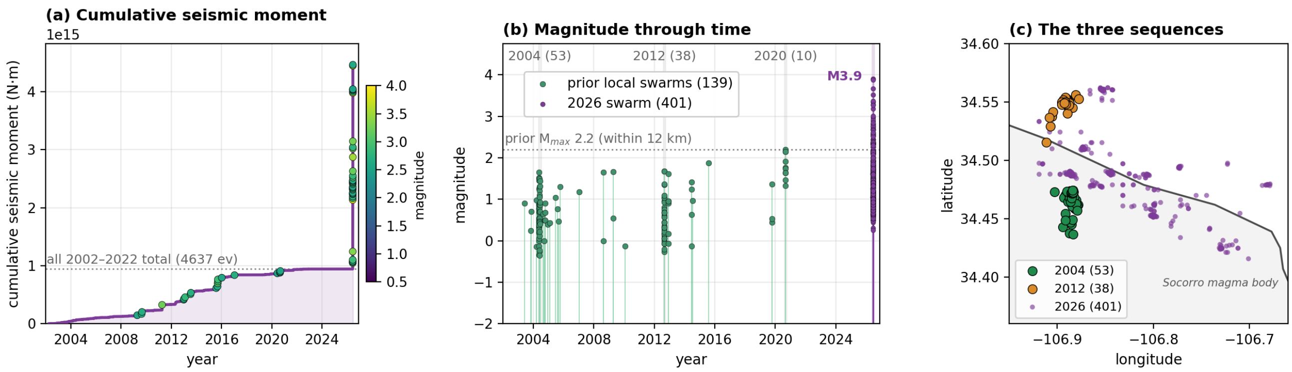

Figure 3 The 2026 swarm against two decades of regional seismicity. (a) Cumulative-moment comparison on the aligned magnitude scale, in which the single 2026 maximum event releases a moment comparable to the cumulative moment of all historical events. (b) Recurrence of swarms within the same accommodation zone in 2004, 2012, and 2026, and the 2026 maximum magnitude against the prior local record. The dotted line is the largest prior event within 12 km of the swarm, M_L 2.2; the region-wide maximum quoted in the text, 2.9, is drawn from the whole 2002 to 2022 catalog and so is larger. (c) Map of the three sequences, which occupy adjacent parts of the accommodation zone rather than a single common structure: the 2004 events near 34.45 to 34.48°N, the 2012 events about 9 km further north, and the 2026 sequence trending west-northwest to east-southeast across and to the east of both. The approximate boundary of the SMB is shown by a black line.

4.2 A low b-value

The 2026 swarm has a b-value near 0.51 (Figure 4a), estimated from the 355 events above the common completeness magnitude of 0.4 on the aligned scale, equivalent to M_L 0.78 on the native 2026 scale. At the swarm's own maximum-curvature M_c of 0.6 the estimate is 0.57, while goodness-of-fit (Wiemer and Wyss, 2000) gives a value of 0.73 on the native scale, and raising M_c raises the estimate steadily, because the frequency-magnitude distribution is curved rather than log-linear (Supplementary Section 3). Gradual curvature of this kind is the shape expected when the completeness magnitude is not uniform across a catalog (Mignan, 2012), and is common in catalogs assembled over long intervals or wide areas. We therefore fix a common M_c across all populations and treat b as a comparative index. Within that convention the largest events do not drive the result. Removing the five largest shifts b by 0.02.

Compared on the aligned magnitude scale at a common completeness magnitude (Figure 4a), the regional background and both prior swarms cluster near a value of 0.8, with the 2004 swarm at 0.88 (0.81 to 0.98), the 2012 swarm at 0.76 (0.67 to 0.87), and the full region at 0.83 (0.82 to 0.85), somewhat above the 0.78 reported for the 2002 to 2009 catalog by Aerts and Bilek (2025). The 2026 swarm is lower at 0.51 (0.49 to 0.53) and stays below the regional 0.83 across the full two-sigma uncertainty of the magnitude scale alignment, ranging from 0.23 to 0.50 as the alignment slope is varied from 0.24 to 1.52.

The result is also independent of the completeness magnitude. The b-positive estimator, which uses positive magnitude differences and needs no completeness threshold to be chosen, though it is not independent of one (Lippiello and Petrillo, 2024), gives 0.59 (0.56 to 0.63) for the 2026 swarm on its native scale, with no alignment applied, against 0.71, 0.92, and 0.75 for the 2004 swarm, the 2012 swarm, and the region respectively (Figure 4a). Because b-positive scales with the slope of any magnitude transformation, the value is 0.52 (0.49 to 0.55) when accounting for the common magnitude scaling; the 2026 swarm remains the lowest population independent of magnitude scaling. The anomaly also holds when examining events at the same depths, with the regional background at 0.91 (0.88 to 0.94) over the 7 to 13 km band that contains the swarm against 0.49 (0.47 to 0.51) for the swarm events in that same band.

Because these distributions are curved, no single b characterizes them, and the comparison is better made at matched magnitude. Where both populations are well sampled the 2026 swarm's local slope is about half the regional value, 0.32 versus 0.59 (magnitudes 0.2 to 0.8), 0.44 versus 0.87 (0.5 to 1.1), and 0.50 versus 1.08 (0.8 to 1.4). The Utsu (1966) test rejects a common b for the two populations at every completeness magnitude from -0.2 to 1.2, with $p < 10^{-10}$ throughout. The contrast is therefore a property of the distributions rather than of the threshold chosen to summarize them (Supplementary Section 3).

4.3 Stress drop relative to the regional baseline

Stress drops for the reliable magnitude range, $M_L \geq 2.5$, have a median near 2.2 MPa from the direct spectral fits (34 events, interquartile range 1.4 to 8.2 MPa), with wide per-event scatter that reflects the known variability of spectral estimates (Figure 4b). The absolute level is limited by the recording bandwidth, since corner frequencies for the smaller events approach the top of the usable band, and the estimates rise steeply with magnitude (correlation 0.68 between $\log_{10} \Delta\sigma$ and M_L within the reliable subset), so the absolute value is uncertain by a large factor. An empirical Green's-function cross-check on co-located high-correlation pairs, which cancels the path and site terms, returns

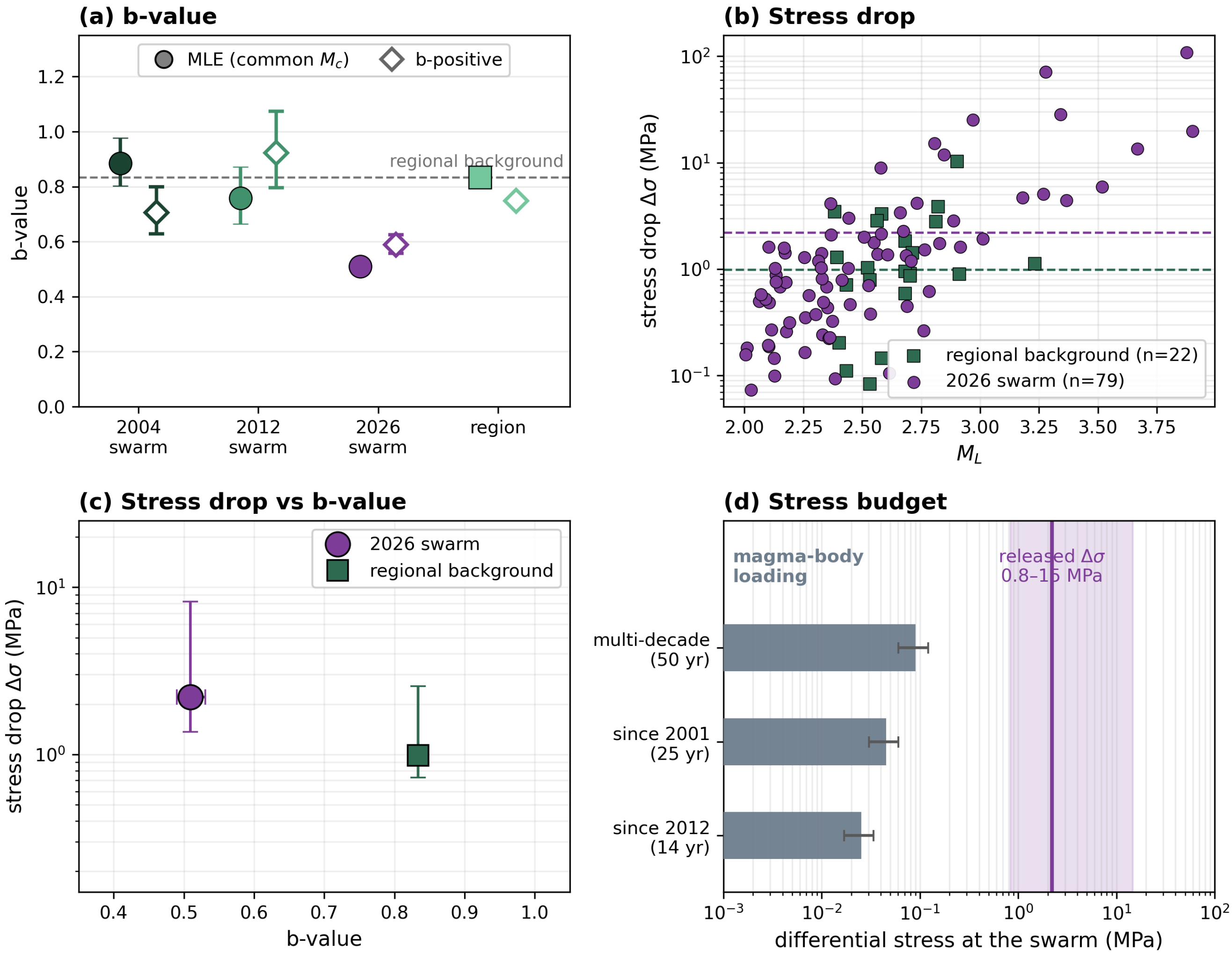

Figure 4 Source physics of the 2026 swarm, consolidating the three source observables and the stress budget. (a) b-value at a common completeness magnitude from the Aki-Utsu maximum-likelihood estimator (filled symbols) and from the b-positive estimator (open diamonds), for the 2004 and 2012 swarms, the 2026 swarm, and the regional background, with the regional value dashed for reference. The 2026 swarm near 0.5 is the low outlier by both estimators. (b) Stress drop against local magnitude for the 2026 swarm and the region-wide events of magnitude 2 and above, processed by the identical method, with the population medians dashed. The swarm's reliable-subset median sits a factor of 2.2 above the regional baseline, and its largest events, whose corner frequencies are the best resolved, reach about 10 MPa. The absolute values are bandwidth-limited. (c) The 2026 swarm and the regional background compared on both source observables at once, the b-value from panel (a) against the median stress drop from panel (b). Horizontal bars are the bootstrap interval on b and vertical bars the interquartile range of the per-event stress drops. The two populations separate on both axes, but only the b-value identifies the driver, because the absolute stress drops of fluid-induced and tectonic earthquakes overlap (Huang et al., 2017) while fluid and magmatic pressurization raises b (Farrell et al., 2009; Glazner and McNutt, 2021) and elevated differential stress lowers it (Scholz, 2015). (d) Stress budget at the swarm. The differential stress imposed by SMB inflation over multi-decadal intervals (bars) is one to two orders of magnitude below the stress released per earthquake (vertical band), so the SMB conditions the crust but does not supply the stress.

higher stress drops than the direct fits for the smaller events, with medians of 2.1 and 0.5 MPa at M_L 2.0 to 2.5, confirming that the direct estimates below M_L 2.5 are suppressed by the bandwidth; estimates below M_L 2.5 are therefore ignored. The largest event passes quality control at eight stations with a stress drop near 20 MPa, and the ten events of $M_L \geq 3$ have a median near 10 MPa.

The meaningful comparison is the ratio with the regional baseline, measured by the same method, not the absolute value. The 22 regional events of magnitude 2 and above have a median stress drop of 1.0 MPa (interquartile range 0.7 to 2.6 MPa) against 2.2 MPa for the swarm's reliable subset, an increase of a factor of 2.2 (Figure 4b). The swarm's largest events carry its highest stress drops, the ten events of $M_L \geq 3$ giving a median of 9.7 MPa with corner frequencies of 4.8 to 14.9 Hz, well inside the usable band. The comparison is nevertheless limited by the composition of the two populations. The regional catalog contains a single event above M_L 3, at 1.1 MPa, so the swarm's largest events have no regional counterpart at matched magnitude.

4.4 Structure and focal mechanisms

The relocated hypocenters occupy an elongate zone above the SMB and resolve into about thirty waveform-similar families (Figure 5a). The swarm lies at mid-crustal depth, roughly 8 to 12 km, with relative depths within each cluster better constrained than absolute ones. The families are not distributed uniformly along the zone but fall into groups that sit near separate mapped fault strands. The zone is narrow across strike, a few kilometers wide (interquartile range 2.8 km, with two families lying about 6 km off the axis), and trends west-northwest to east-southeast, within a few degrees of the network's least-resolved direction (Figure 5b, c). With stations only at northerly and southerly azimuths, east-west relative positions are roughly twice as poorly constrained as north-south, so the along-trend extent, the obliquity to the rift, and the fault dip are not well resolved. The regional moment tensor of the largest event gives normal to oblique-normal faulting, and the full moment tensor from the local first-motion data bounds its isotropic component at $+8$ percent of the total moment (90 percent interval -22 to $+36$ percent), which excludes a dominant volumetric source although it would not resolve a small one. For the ten events of magnitude 3 and above, adding the western Arizona polarities reduces the first-motion solution space by 56 percent per event on average (60 percent in aggregate), but the acceptable solution space is large, so the smaller events are not individually well resolved. Seven of the ten have a preferred normal mechanism and three a preferred strike-slip mechanism, consistent with but not uniquely resolving the normal faulting of the largest event (Figure 6). Faulting style here is assigned from the plunge of the P and T axes with a 50 degree threshold, so an event with an oblique rake can fall either side of the boundary on a small change of solution. The ten events span the swarm volume, at depths of 8.2 to 12.9 km and M_L 3.0 to 3.9 (network magnitudes 3.1 to 3.9), with a median separation between event pairs of 8.4 km. The three events carrying a preferred strike-slip solution span 9.0 to 12.3 km in depth and are separated from one another by 6.5 km at the median. Per-event parameters and resolution statistics are given in Supplementary Table S1. The 2004 and 2012 swarms are below the magnitude at which mechanisms can be resolved, so we do not assign mechanisms to them.

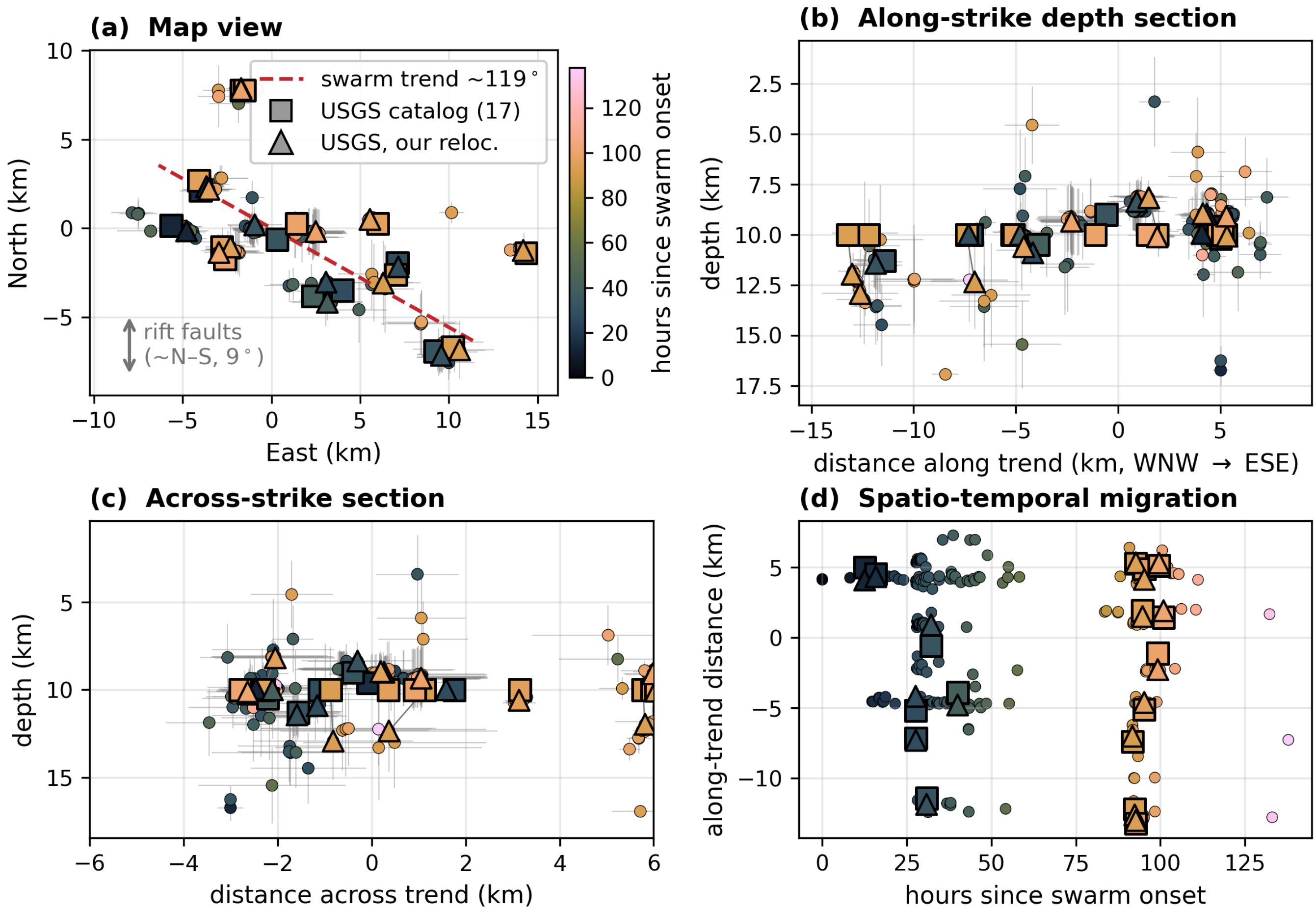

Figure 5 Hypocentral structure of the relocated swarm, all panels colored by time since swarm onset, where onset is the first detected event of the sequence. (a) Map view, with the fitted swarm trend near 119 degrees and the near-north strike of the mapped rift faults shown for comparison. (b) Depth section along that trend, from west-northwest to east-southeast. (c) Depth section across the trend, showing a core only a few kilometers wide. (d) Along-trend position against time, in which the families activate in two bursts separated by a quiescent interval. The hypocenters lie at mid-crustal depths of roughly 8 to 12 km, although the absolute depth is poorly resolved, and the apparent west-northwest to east-southeast elongation lies along the network's least-resolved direction, so its extent and orientation are not well constrained. Small circles are the individual relocated detections. Squares are USGS catalog events (U.S. Geological Survey, 2017) and triangles our relocations of them. Gray bars are per-event GrowClust bootstrap location uncertainties, drawn for every relocated event shown at the 95th percentile of the bootstrap resample deviation, with median values over the events shown of 658 m east, 315 m north and 785 m in depth. Bars are longer east-west than north-south because the network samples only northerly and southerly azimuths, which is why we do not interpret the along-trend extent or the obliquity of the zone to the rift.

4.5 Spatio-temporal character

GrowClust resolves the sequence into about thirty waveform-similar families (Figure 7a), and their activation is episodic and spatially disordered. The swarm families activate within hours of the first event and out of order, in two bursts separated by a quiescent interval (Figure 7b). We also fit a diffusion curve to check the plausibility of fluid triggering. Here, the migration is non-monotonic and bimodal rather than ordered. A diffusion front for this swarm would also require a hydraulic diffusivity of order tens of square meters per second or more, whereas fluid-driven and induced sequences typically require 0.1 to 10 m^2/s (Shapiro et al., 1997; Talwani et al., 2007; Figure 7c). The inter-family distances are measured along the least-resolved direction, which makes the diffusivity more uncertain, but the disordered, two-burst timing is independent of that uncertainty.

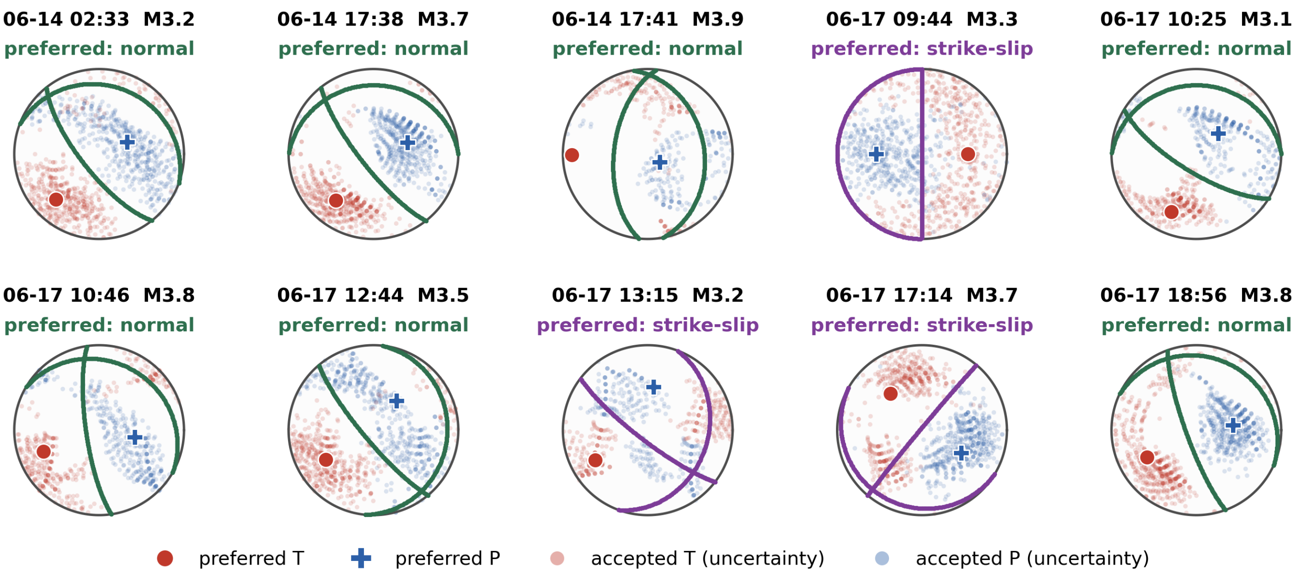

Figure 6 First-motion focal-mechanism solution spaces for the ten events of magnitude 3 and above, with the western Arizona polarities added. Each focal sphere shows the preferred mechanism (nodal planes and preferred P and T axes) and the cloud of acceptable mechanisms, with the preferred faulting style labeled above. Seven of the ten preferred mechanisms are normal and the other three strike-slip, consistent with the largest event, whose mechanism is fixed to its USGS regional moment tensor (U.S. Geological Survey, 2017). The acceptable clouds are broad, set by the unsampled eastern azimuth, so the individual mechanisms are only weakly constrained; we rely on the regional moment tensor of the largest event for the definitive normal mechanism.

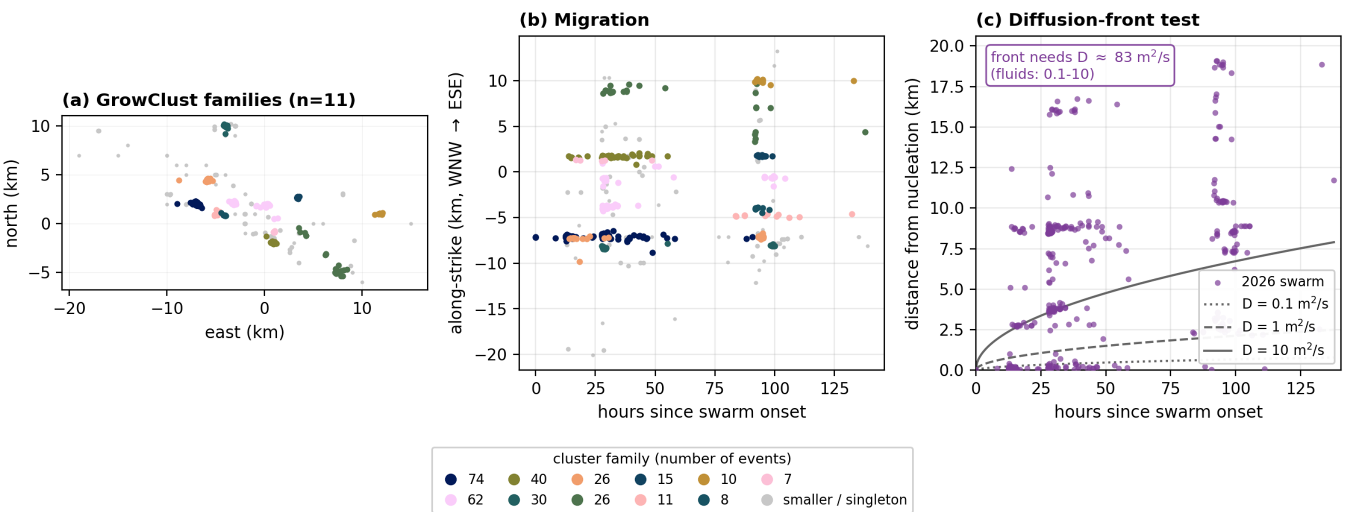

Figure 7 Spatio-temporal character of the swarm. (a) GrowClust families, the eleven with at least five events colored with the batlowS categorical colormap and smaller or unclustered events in gray. (b) Position along the apparent trend against time, with distinct families activating within hours and out of order, in two bursts. (c) Distance from the nucleation against time, with pore-pressure diffusion fronts $r = \sqrt{4\pi Dt}$. The migration is non-monotonic and bimodal, unlike a diffusing front, and would require a diffusivity of tens of m^2/s or more, above the 0.1 to 10 m^2/s of fluid-driven seismicity (Shapiro et al., 1997; Talwani et al., 2007).

4.6 Stress from SMB uplift

The SMB cannot directly supply the stress the swarm released (Figure 4d). Modeled as a Mogi center of dilatation at 19 km depth and calibrated to the observed surface uplift, the SMB imposes a differential stress at the swarm hypocenter of order one kilopascal per year. Over the 50 years of monitored inflation this amounts to only about 0.03 to 0.1 MPa. This loading rate is of the same order as the roughly 0.6 kilopascals per year increase in magma overpressure inferred for the sill (Fialko et al., 2001), though that is a reservoir overpressure rather than a differential stress at the source. The stress released per earthquake, even at the low end of the stress-drop estimates, is one to two orders of magnitude larger. The differential stress that the swarm relieved is likely tectonic in origin, and the SMB sets the thermal state but does not drive the seismicity.

5 Discussion

The source-physics observables support our interpretation of non-magmatic tectonic faulting. The low b-value indicates a highly stressed volume, and the stress drops, which exceed the regional baseline by a factor of two and reach about 10 MPa in the largest events, show that the ruptures released stress efficiently rather than showing the reduced stress drops that fluid-weakened faults can produce. The normal double-couple mechanism, with no resolvable isotropic component, indicates shear failure without a volumetric component. Together these provide evidence that the 2026 swarm is in the high-differential-stress regime, distinct from fluid-driven swarms, which have high b-values (Farrell et al., 2009; Glazner and McNutt, 2021) and frequent non-double-couple components (Miller et al., 1998; Figure 4c).

We interpret the swarm as the activation of the San Acacia accommodation zone, the transverse belt that transfers extension between the Socorro and Albuquerque-Belen basins (Grauch and Connell, 2013; Sion et al., 2020). Accommodation zones of this kind are structurally complex belts of distributed, segment-linking normal faulting (Chapin and Cather, 1994), where stress concentrates at fault overlaps and relay structures, and they localize seismicity. The magnitude 4.2 San Acacia swarm of 1983 occurred on this same zone (Sanford et al., 1995), and the 2004, 2012, and 2026 sequences recur within it. Whether the earlier sequences shared the 2026 mechanism is below what their magnitudes allow us to resolve. The normal-faulting mechanism, accommodating the same east-west extension that drives the rift, places the 2026 swarm among these rift-parallel faults.

The episodic, spatially disordered activation of the swarm, with no diffusive migration front, is the signature of tectonic failure rather than a fluid or aseismic driver, consistent with ordinary tectonic loading of the accommodation zone. This reframes the role of the SMB. The melt warms and weakens the crust, and the SMB inflates steadily through the study period (Figure 2), but steady inflation is not the same as driving the seismicity. Active magma or fluid movement is usually expressed as deep long-period events depleted in high frequencies (Aki and Koyanagi, 1981; Nichols et al., 2011), and slow slip as families of quasi-periodic repeating earthquakes (Nadeau and McEvilly, 1999; Uchida and Bürgmann, 2019). The detected events are uniformly high-frequency, with a median frequency index of $+0.89$ and no dependence on depth, and a waveform-similarity search finds no quasi-periodic repeaters, so neither active fluid or magma movement nor aseismic creep is expressed in the detected seismicity. This interpretation is consistent with the 2009 microearthquake swarm above the SMB, for which Ruhl et al. (2010) attributed a rift-like b-

value and regionally consistent focal mechanisms to failure of the pre-existing fractured crust rather than to magma movement. It departs from the classic interpretation of the Socorro seismicity, which ascribes the microearthquakes to stresses imposed by the inflating body (Sanford et al., 1977).

Aerts and Bilek (2025) present the most recent characterization of the SMB seismicity, relocating the 2002 to 2009 catalog and attributing the clusters and swarms to rupture of pre-existing rift faults triggered by fluid-pressure pulses. They base this interpretation on highly correlated waveforms, day-scale durations, and the few sequences whose fronts migrate at hydraulic diffusivities of 1 to 10 m^2/s. Most of the swarms, however, lack a migration front and exhibit b-values near 0.8, with predominantly normal focal mechanisms. The scarcity of repeating earthquakes and of steady seismicity rates further led the authors to discount aseismic slip. Within this spectrum, the 2026 swarm represents the tectonic end-member. The b-value of 0.51 lies below the 0.78 of the full 2002 to 2009 catalog, the stress drops exceed the regional baseline by a factor of two and reach about 10 MPa in the largest events, and the hypocenters spread too rapidly to match the 1 to 10 m^2/s pore-pressure fronts of those sequences. We therefore interpret the 2026 sequence as a tectonic, high-differential-stress episode rather than a larger counterpart of the region's fluid-triggered swarms.

Several limitations constrain our analysis. The sparse and azimuthally incomplete network limits the resolution of small-event mechanisms, and only the largest event has a well-resolved moment tensor. The absolute depths are also poorly resolved, because all stations lie at the surface and source depth is strongly correlated with origin time in the location, so the swarm centroid near 8 to 12 km retains a large systematic uncertainty even where the relative depths within the clusters are well constrained. Reflected phases from the SMB could provide independent depth control, since the mid-crustal reflections that first revealed the body (Sanford et al., 1977) traverse the crust beneath the seismicity and the delay of a phase reflected from the sill near 19 km relative to the direct arrival depends on source depth. A search for such phases lies beyond the scope of this study but would supply the absolute depth control that a surface network alone cannot provide. The recording bandwidth restricts reliable stress drops to events above M_L 2.5, and we therefore report only that subset and use relative rather than absolute values. The historical stress-drop baseline rests on the larger region-wide events because the prior swarms are too small for spectral fitting. Our statement that the sequence contains no low-frequency population applies to the detected events only. We did not run a dedicated search of the continuous record for deep long-period events, and a matched filter built from ordinary local earthquakes and run in a 2 to 12 Hz band would not detect them, so we cannot exclude a low-frequency population at the depth of the sill. The magnitude-scale frequency-magnitude distributions are curved rather than log-linear, so no single b characterizes them and the value we quote depends on the threshold at which it is measured; the contrast between populations does not, and is preserved at matched magnitude and under every estimator we applied. The magnitude-scale alignment carries a residual slope uncertainty, although the b-value anomaly is robust both to that uncertainty and to the scale-independent b-positive estimator. The stress-drop comparison is limited on the regional side by the scarcity of events above M_L 3, so the swarm's largest events have no regional counterpart at matched magnitude, and because stress drop rises steeply with magnitude in both populations, and the two populations sample different depths, the elevation we report cannot be attributed to the sources alone. None of these limitations affects the central result, which uses the joint interpretation of an M_c-independent low b-value, elevated stress drops, and a normal double-couple mechanism.

These results identify the San Acacia accommodation zone as a persistent source of the region's larger earthquakes. The zone has generated two earthquakes near magnitude 4, the 2026 sequence at M_L 3.9 and the 1983 event at magnitude 4.2, both exceeding the maximum of 2.9 in the modern instrumental record; hazard assessments based on that record alone therefore underestimate the maximum magnitude of this structure. The sparse regional network constrains the frequency-magnitude distribution only coarsely, and a denser local deployment would sharpen every number reported here. Because the sequence is tectonic rather than magmatic, the hazard is related to rift faulting and does not represent unrest of the underlying magma body, a distinction relevant wherever seismicity above a magma body could otherwise be interpreted as a volcanic precursor.

6 Conclusions

The June 2026 Socorro swarm has a b-value near 0.51, low relative to a regional background near 0.83 and to two earlier swarms within the same accommodation zone when all are compared at a common completeness magnitude of 0.4 on a consistent magnitude scale, and stress drops about twice a regional baseline measured by the same method, with the largest events reaching about 10 MPa. The b-value contrast persists under the b-positive estimator, and across the full two-sigma uncertainty of the magnitude-scale alignment. The largest event has a normal mechanism with no resolvable isotropic component, and the smaller events, though weakly constrained, are consistent with normal faulting. The waveform-similar families activate episodically and out of spatial order, with no diffusive migration front and require a rate too rapid for fluid pressurization. The steady inflation of the underlying magma body supplies only about 0.03 to 0.1 MPa of differential stress at the source, one to two orders of magnitude below the stress released per event. Together these observables identify non-magmatic, high-differential-stress faulting rather than a fluid or magmatic process, and we interpret the sequence as a reactivation of the San Acacia accommodation zone under ordinary tectonic loading. This zone is a persistent source of the region's larger earthquakes, with both the 2026 sequence and the magnitude 4.2 earthquake of 1983 occurring on this structure.

Seismicity above the Socorro Magma Body has been attributed both to stresses imposed by the inflating sill (Sanford et al., 1977) and, more recently, to fluid-pressure pulses on pre-existing rift faults (Aerts and Bilek, 2025). In this context, the 2026 sequence represents the tectonic end-member, in which earthquakes are predominantly driven by rift-related rupture rather than the SMB.

Acknowledgements

The authors thank the operators of the contributing seismic networks and the EarthScope FDSN data services. Data were accessed from the NSF NGF data archive operated by EarthScope Consortium (NSF award 2435260).

Data and code availability

Seismic waveforms and instrument metadata were obtained through EarthScope FDSN web services from the Global Seismograph Network (IU; Albuquerque Seismological Laboratory/USGS 1988), the US Geological Survey Networks (GS; Albuquerque Seismological Laboratory (ASL)/USGS 1980), the New Mexico Tech Seismic Network (SC; New Mexico Tech 1999), the Arizona Broadband Seismic Network (AE; Arizona Geological Survey 2007), the USArray Transportable Array (TA; IRIS Transportable Array 2003), and the Bedload Monitoring of Ephemeral Streams network (X9; Bilek 2019), and from the Raspberry Shake FDSN web service for the Raspberry Shake network (AM; Raspberry Shake, S.A. 2016). Catalog hypocenters and network magnitudes, and the regional moment tensor of the largest event, were obtained from the ANSS Comprehensive Catalog (ComCat; U.S. Geological Survey 2017). Processed continuous waveforms of the five effective stations and response metadata from the SmartSolo nodal array are archived in a public Zenodo repository (Calvelage et al., 2026). The InSAR velocities and time series come from the OPERA DISP-S1 product (NASA/JPL/OPERA, 2025), distributed by the Alaska Satellite Facility DAAC, and contain modified Copernicus Sentinel-1 data (2016–2025). The relocation used GrowClust3D.jl (Trugman et al., 2023), the first-motion mechanisms SKHASH (Skoumal et al., 2024), the full moment tensors MTfit (Pugh and White, 2018), and the regional moment-tensor check Computer Programs in Seismology (Herrmann, 2013). The remaining analysis was performed with open-source scientific Python libraries, ObsPy (Krischer et al., 2015), NumPy (Harris et al., 2020), SciPy (Virtanen et al., 2020), and Matplotlib (Hunter, 2007). Maps were drawn with Cartopy (Elson et al., 2023), and the figures use the scientific color maps (Crameri, 2023; Crameri et al., 2020). The relocated event catalog, local magnitudes, focal mechanisms, and source-parameter tables are archived in the same Zenodo repository.

Competing interests

The authors declare no competing interests.

References

Abercrombie, R. E. Earthquake source scaling relationships from -1 to 5 M_L using seismograms recorded at 2.5-km depth. *Journal of Geophysical Research: Solid Earth*, 100(B12):24015–24036, 1995. doi: 10.1029/95JB02397.

Aerts, J. R. *Earthquake relocation and characterization methods and their application to the area above the Socorro magma body in Central New Mexico and to icequake swarms in the Beaufort Sea*. Doctoral dissertation, New Mexico Institute of Mining and Technology, 2024.

Aerts, J. R. and Bilek, S. L. Characterization of earthquake clustering and swarms in Central New Mexico from 2002–2009 associated with the Socorro Magma Body. *Bulletin of the Seismological Society of America*, 115(1):115–129, 2025. doi: 10.1785/0120240032.

Aki, K. Maximum likelihood estimate of b in the formula $\log N = a - bM$ and its confidence limits. *Bulletin of the Earthquake Research Institute, University of Tokyo*, 43(2):237–239, 1965. doi: 10.15083/0000033631.

Aki, K. and Koyanagi, R. Deep volcanic tremor and magma ascent mechanism under Kilauea, Hawaii. *Journal of Geophysical Research: Solid Earth*, 86(B8):7095–7109, 1981. doi: 10.1029/JB086iB08p07095.

Albuquerque Seismological Laboratory (ASL)/USGS. US Geological Survey Networks [Data set]. International Federation of Digital Seismograph Networks, 1980. doi: 10.7914/SN/GS.

Albuquerque Seismological Laboratory/USGS. Global Seismograph Network (GSN - IRIS/USGS) [Data set]. International Federation of Digital Seismograph Networks, 1988. doi: 10.7914/SN/IU.

Allmann, B. P. and Shearer, P. M. Global variations of stress drop for moderate to large earthquakes. *Journal of Geophysical Research: Solid Earth*, 114(B1):B01310, 2009. doi: 10.1029/2008JB005821.

Arizona Geological Survey. Arizona Broadband Seismic Network [Data set]. International Federation of Digital Seismograph Networks, 2007. doi: 10.7914/SN/AE.

Balch, R. S., Hartse, H. E., Sanford, A. R., and Lin, K.-W. A new map of the geographic extent of the Socorro mid-crustal magma body. *Bulletin of the Seismological Society of America*, 87(1):174–182, 1997. doi: 10.1785/BSSA0870010174.

Bilek, S. Bedload Monitoring of Ephemeral Streams (seed) [Data set]. International Federation of Digital Seismograph Networks, 2019. doi: 10.7914/SN/X9_2019.

Brune, J. N. Tectonic stress and the spectra of seismic shear waves from earthquakes. *Journal of Geophysical Research*, 75(26):4997–5009, 1970. doi: 10.1029/JB075i026p04997.

Calvelage, C. M., Aerts, J. R., Bilek, S. L., and Basu, U. Data for: The June 2026 Socorro swarm: A reactivation of rift-parallel normal faults above the Socorro Magma Body [Data set]. Zenodo, 2026. doi: 10.5281/zenodo.22964370.

Chamberlin, R. M. Geologic map, cross section, and map units of the Lemitar Mountains, Socorro County, New Mexico. Open-File Report 169, New Mexico Bureau of Geology and Mineral Resources, 1982. doi: 10.58799/OFR-169. Scale 1:12,000.

Chapin, C. E. and Cather, S. M. Tectonic setting of the axial basins of the northern and central Rio Grande rift. In Keller, G. R. and Cather, S. M., editors, *Basins of the Rio Grande rift: Structure, stratigraphy, and tectonic setting*, number 291 in Geological Society of America Special Papers, pages 5–26. Geological Society of America, 1994. doi: 10.1130/SPE291-p5.

Crameri, F. Scientific colour maps (Version 8.0.0) [Computer software]. Zenodo, 2023. doi: 10.5281/zenodo.8035877.

Crameri, F., Shephard, G. E., and Heron, P. J. The misuse of colour in science communication. *Nature Communications*, 11(1):5444, 2020. doi: 10.1038/s41467-020-19160-7.

Danré, P., Garagash, D., De Barros, L., Cappa, F., and Ampuero, J.-P. Control of seismicity migration in earthquake swarms by injected fluid volume and aseismic crack propagation. *Journal of Geophysical Research: Solid Earth*, 129(1):e2023JB027276, 2024. doi: 10.1029/2023JB027276.

Elson, P., Sales de Andrade, E., Lucas, G., May, R., Hattersley, R., Campbell, E., Dawson, A., Little, B., Raynaud, S., scmc72, Snow, A. D., Comer, R., Donkers, K., Blay, B., Killick, P., Wilson, N., Peglar, P., lgolston, lbdreyer, Andrew, Szymaniak, J., Berchet, A., Bosley, C., Davis, L., Filipe, Krasting, J., Bradbury, M., Kirkham, D., stephenworsley, and Havlin, C. Cartopy: A cartographic Python library with a Matplotlib interface (Version 0.22.0) [Computer software]. Zenodo, 2023. doi: 10.5281/zenodo.1182735.

Farrell, J., Husen, S., and Smith, R. B. Earthquake swarm and b-value characterization of the Yellowstone volcano-tectonic system. *Journal of Volcanology and Geothermal Research*, 188(1-3):260–276, 2009. doi: 10.1016/j.jvolgeores.2009.08.008.

Faulds, J. E. and Varga, R. J. The role of accommodation zones and transfer zones in the regional segmentation of extended terranes. In Faulds, J. E. and Stewart, J. H., editors, *Accommodation zones and transfer zones: The regional segmentation of the Basin and Range province*, number 323 in Geological Society of America Special Papers, pages 1–46. Geological Society of America, 1998. doi: 10.1130/0-8137-2323-X.1.

Fialko, Y. and Simons, M. Evidence for on-going inflation of the Socorro magma body, New Mexico, from interferometric synthetic aperture radar imaging. *Geophysical Research Letters*, 28(18):3549–3552, 2001. doi: 10.1029/2001GL013318.

Fialko, Y., Simons, M., and Khazan, Y. Finite source modelling of magmatic unrest in Socorro, New Mexico, and Long Valley, California. *Geophysical Journal International*, 146(1):191–200, 2001. doi: 10.1046/j.1365-246X.2001.00453.x.

Glazner, A. F. and McNutt, S. R. Relationship between dike injection and b-value for volcanic earthquake swarms. *Journal of Geophysical Research: Solid Earth*, 126(12):e2020JB021631, 2021. doi: 10.1029/2020JB021631.

Grauch, V. J. S. and Connell, S. D. New perspectives on the geometry of the Albuquerque Basin, Rio Grande rift, New Mexico: Insights from geophysical models of rift-fill thickness. In Hudson, M. R. and Grauch, V. J. S., editors, *New perspectives on Rio Grande rift basins: From tectonics to groundwater*, number 494 in Geological Society of America Special Papers, pages 427–462. Geological Society of America, 2013. doi: 10.1130/2013.2494(16).

Hardebeck, J. L. and Shearer, P. M. A new method for determining first-motion focal mechanisms. *Bulletin of the Seismological Society of America*, 92(6):2264–2276, 2002. doi: 10.1785/0120010200.

Harris, C. R., Millman, K. J., van der Walt, S. J., Gommers, R., Virtanen, P., Cournapeau, D., Wieser, E., Taylor, J., Berg, S., Smith, N. J., Kern, R., Picus, M., Hoyer, S., van Kerkwijk, M. H., Brett, M., Haldane, A., del Río, J. F., Wiebe, M., Peterson, P., Gérard-Marchant, P., Sheppard, K., Reddy, T., Weckesser, W., Abbasi, H., Gohlke, C., and Oliphant, T. E. Array programming with NumPy. *Nature*, 585(7825):357–362, 2020. doi: 10.1038/s41586-020-2649-2.

Heidbach, O., Rajabi, M., Cui, X., Fuchs, K., Müller, B., Reinecker, J., Reiter, K., Tingay, M., Wenzel, F., Xie, F., Ziegler, M. O., Zoback, M.-L., and Zoback, M. The World Stress Map database release 2016: Crustal stress pattern across scales. *Tectonophysics*, 744:484–498, 2018. doi: 10.1016/j.tecto.2018.07.007.

Heilman, E., Kolawole, F., Atekwana, E. A., and Mayle, M. Controls of basement fabric on the linkage of rift segments. *Tectonics*, 38(4): 1337–1366, 2019. doi: 10.1029/2018TC005362.

Herrmann, R. B. Computer programs in seismology: An evolving tool for instruction and research. *Seismological Research Letters*, 84(6): 1081–1088, 2013. doi: 10.1785/0220110096.

Huang, Y., Ellsworth, W. L., and Beroza, G. C. Stress drops of induced and tectonic earthquakes in the central United States are indistinguishable. *Science Advances*, 3(8):e1700772, 2017. doi: 10.1126/sciadv.1700772.

Hunter, J. D. Matplotlib: A 2D graphics environment. *Computing in Science & Engineering*, 9(3):90–95, 2007. doi: 10.1109/MCSE.2007.55.

IRIS Transportable Array. USArray Transportable Array [Data set]. International Federation of Digital Seismograph Networks, 2003. doi: 10.7914/SN/TA.

Krischer, L., Megies, T., Barsch, R., Beyreuther, M., Lecocq, T., Caudron, C., and Wassermann, J. ObsPy: A bridge for seismology into the scientific Python ecosystem. *Computational Science & Discovery*, 8(1):014003, 2015. doi: 10.1088/1749-4699/8/1/014003.

Lippiello, E. and Petrillo, G. b-more-incomplete and b-more-positive: Insights on a robust estimator of magnitude distribution. *Journal of Geophysical Research: Solid Earth*, 129(2):e2023JB027849, 2024. doi: 10.1029/2023JB027849.

Lohman, R. B. and McGuire, J. J. Earthquake swarms driven by aseismic creep in the Salton Trough, California. *Journal of Geophysical Research: Solid Earth*, 112(B4):B04405, 2007. doi: 10.1029/2006JB004596.

Mignan, A. Functional shape of the earthquake frequency-magnitude distribution and completeness magnitude. *Journal of Geophysical Research: Solid Earth*, 117(B8):B08302, 2012. doi: 10.1029/2012JB009347.

Miller, A. D., Foulger, G. R., and Julian, B. R. Non-double-couple earthquakes 2. Observations. *Reviews of Geophysics*, 36(4):551–568, 1998. doi: 10.1029/98RG00717.

Minor, S. A., Hudson, M. R., Caine, J. S., and Thompson, R. A. Oblique transfer of extensional strain between basins of the middle Rio Grande rift, New Mexico: Fault kinematic and paleostress constraints. In Hudson, M. R. and Grauch, V. J. S., editors, *New perspectives on Rio Grande rift basins: From tectonics to groundwater*, number 494 in Geological Society of America Special Papers, pages 345–382. Geological Society of America, 2013. doi: 10.1130/2013.2494(14).

Murray, K. D., Murray, M. H., and Sheehan, A. F. Active deformation near the Rio Grande Rift and Colorado Plateau as inferred from continuous Global Positioning System measurements. *Journal of Geophysical Research: Solid Earth*, 124(2):2166–2183, 2019. doi: 10.1029/2018JB016626.

Nadeau, R. M. and McEvilly, T. V. Fault slip rates at depth from recurrence intervals of repeating microearthquakes. *Science*, 285(5428): 718–721, 1999. doi: 10.1126/science.285.5428.718.

Nakai, J. S., Sheehan, A. F., and Bilek, S. L. Seismicity of the Rocky Mountains and Rio Grande Rift from the EarthScope Transportable Array and CREST temporary seismic networks, 2008–2010. *Journal of Geophysical Research: Solid Earth*, 122(3):2173–2192, 2017. doi: 10.1002/2016JB013389.

NASA/JPL/OPERA. OPERA Surface Displacement from Sentinel-1 validated product (Version 1) [Data set]. NASA Alaska Satellite Facility Distributed Active Archive Center, 2025. doi: 10.5067/SNWG/OPL3DISPS1-V1.

New Mexico Tech. New Mexico Tech Seismic Network [Data set]. International Federation of Digital Seismograph Networks, 1999. doi: 10.7914/0abk-1345.

Nichols, M. L., Malone, S. D., Moran, S. C., Thelen, W. A., and Vidale, J. E. Deep long-period earthquakes beneath Washington and Oregon volcanoes. *Journal of Volcanology and Geothermal Research*, 200(3-4):116–128, 2011. doi: 10.1016/j.jvolgeores.2010.12.005.

Page, R. Aftershocks and microaftershocks of the great Alaska earthquake of 1964. *Bulletin of the Seismological Society of America*, 58(3): 1131–1168, 1968.

Pugh, D. J. and White, R. S. MTfit: A Bayesian approach to seismic moment tensor inversion. *Seismological Research Letters*, 89(4):1507–1513, 2018. doi: 10.1785/0220170273.

Raspberry Shake, S.A. Raspberry Shake [Data set]. International Federation of Digital Seismograph Networks, 2016. doi: 10.7914/SN/AM.

Rinehart, E. J., Sanford, A. R., and Ward, R. M. Geographic extent and shape of an extensive magma body at mid-crustal depths in the Rio Grande rift near Socorro, New Mexico. In Riecker, R. E., editor, *Rio Grande rift: Tectonics and magmatism*, pages 237–252. American Geophysical Union, 1979. doi: 10.1029/SP014p0237.

Roberts, N. S., Bell, A. F., and Main, I. G. Are volcanic seismic b-values high, and if so when? *Journal of Volcanology and Geothermal Research*, 308:127–141, 2015. doi: 10.1016/j.jvolgeores.2015.10.021.

Roland, E. and McGuire, J. J. Earthquake swarms on transform faults. *Geophysical Journal International*, 178(3):1677–1690, 2009. doi: 10.1111/j.1365-246X.2009.04214.x.

Ruhl, C. J., Bilek, S. L., and Stankova-Pursley, J. Relocation and characterization of the August 2009 microearthquake swarm above the Socorro magma body in the central Rio Grande rift. *Geophysical Research Letters*, 37(23):L23304, 2010. doi: 10.1029/2010GL045162.

Sanford, A. R., Mott, R. P., Shuleski, P. J., Rinehart, E. J., Caravella, F. J., Ward, R. M., and Wallace, T. C. Geophysical evidence for a magma body in the crust in the vicinity of Socorro, New Mexico. In Heacock, J. G., Keller, G. V., Oliver, J. E., and Simmons, G., editors, *The Earth's crust: Its nature and physical properties*, number 20 in Geophysical Monograph Series, pages 385–403. American Geophysical Union, 1977. doi: 10.1029/GM020p0385.

Sanford, A. R., Balch, R. S., House, L. S., and Hartse, H. E. Investigation of rifting processes in the Rio Grande rift using data from unusually large earthquake swarms. Technical Report LA-SUB-95-135, Los Alamos National Laboratory and New Mexico Institute of Mining and Technology, 1995. doi: 10.2172/148695.

Scholz, C. H. On the stress dependence of the earthquake b value. *Geophysical Research Letters*, 42(5):1399–1402, 2015. doi: 10.1002/2014GL062863.

Schorlemmer, D., Wiemer, S., and Wyss, M. Variations in earthquake-size distribution across different stress regimes. *Nature*, 437(7058): 539–542, 2005. doi: 10.1038/nature04094.

Shapiro, S. A., Huenges, E., and Borm, G. Estimating the crust permeability from fluid-injection-induced seismic emission at the KTB site. *Geophysical Journal International*, 131(2):F15–F18, 1997. doi: 10.1111/j.1365-246X.1997.tb01215.x.

Shelly, D. R., Ellsworth, W. L., and Hill, D. P. Fluid-faulting evolution in high definition: Connecting fault structure and frequency-magnitude variations during the 2014 Long Valley Caldera, California, earthquake swarm. *Journal of Geophysical Research: Solid Earth*, 121(3): 1776–1795, 2016. doi: 10.1002/2015JB012719.

Shi, Y. and Bolt, B. A. The standard error of the magnitude-frequency b value. *Bulletin of the Seismological Society of America*, 72(5):1677–1687, 1982. doi: 10.1785/BSSA0720051677.

Sion, B. D., Phillips, F. M., Axen, G. J., Harrison, J. B. J., Love, D. W., and Zimmerer, M. J. Chronology of terraces in the Rio Grande rift, Socorro basin, New Mexico: Implications for terrace formation. *Geosphere*, 16(6):1457–1478, 2020. doi: 10.1130/ges02220.1.

Skoumal, R. J., Hardebeck, J. L., and Shearer, P. M. SKHASH: A Python package for computing earthquake focal mechanisms. *Seismological Research Letters*, 95(4):2519–2526, 2024. doi: 10.1785/0220230329.

Stankova, J., Bilek, S. L., Rowe, C. A., and Aster, R. C. Characteristics of the October 2005 microearthquake swarm and reactivation of similar event seismic swarms over decadal time periods near Socorro, New Mexico. *Bulletin of the Seismological Society of America*, 98(1):93–105, 2008. doi: 10.1785/0120070108.

Talwani, P., Chen, L., and Gahalaut, K. Seismogenic permeability, k_s. *Journal of Geophysical Research: Solid Earth*, 112(B7):B07309, 2007. doi: 10.1029/2006JB004665.

Trugman, D. T. and Shearer, P. M. GrowClust: A hierarchical clustering algorithm for relative earthquake relocation, with application to the Spanish Springs and Sheldon, Nevada, earthquake sequences. *Seismological Research Letters*, 88(2A):379–391, 2017. doi: 10.1785/0220160188.

Trugman, D. T., Chamberlain, C. J., Savvaidis, A., and Lomax, A. GrowClust3D.jl: A Julia package for the relative relocation of earthquake hypocenters using 3D velocity models. *Seismological Research Letters*, 94(1):443–456, 2023. doi: 10.1785/0220220193.

Uchida, N. and Bürgmann, R. Repeating earthquakes. *Annual Review of Earth and Planetary Sciences*, 47:305–332, 2019. doi: 10.1146/annurev-earth-053018-060119.

U.S. Geological Survey. Advanced National Seismic System (ANSS) Comprehensive Catalog [Data set], 2017. doi: 10.5066/F7MS3QZH.

U.S. Geological Survey. Quaternary Fault and Fold Database for the Nation [Data set], 2020. doi: 10.5066/P9BCVRCK. Accessed June 15, 2026.

Utsu, T. A statistical significance test of the difference in b-value between two earthquake groups. *Journal of Physics of the Earth*, 14(2): 37–40, 1966. doi: 10.4294/jpe1952.14.37.

van der Elst, N. J. *B*-positive: A robust estimator of aftershock magnitude distribution in transiently incomplete catalogs. *Journal of Geophysical Research: Solid Earth*, 126(2):e2020JB021027, 2021. doi: 10.1029/2020JB021027.

Virtanen, P., Gommers, R., Oliphant, T. E., Haberland, M., Reddy, T., Cournapeau, D., Burovski, E., Peterson, P., Weckesser, W., Bright, J., van der Walt, S. J., Brett, M., Wilson, J., Millman, K. J., Mayorov, N., Nelson, A. R. J., Jones, E., Kern, R., Larson, E., Carey, C. J., Polat, İ., Feng, Y., Moore, E. W., VanderPlas, J., Laxalde, D., Perktold, J., Cimrman, R., Henriksen, I., Quintero, E. A., Harris, C. R., Archibald, A. M., Ribeiro, A. H., Pedregosa, F., van Mulbregt, P., and SciPy 1.0 Contributors. SciPy 1.0: Fundamental algorithms for scientific computing in Python. *Nature Methods*, 17(3):261–272, 2020. doi: 10.1038/s41592-019-0686-2.

Waldhauser, F. and Ellsworth, W. L. A double-difference earthquake location algorithm: Method and application to the northern Hayward fault, California. *Bulletin of the Seismological Society of America*, 90(6):1353–1368, 2000. doi: 10.1785/0120000006.

Wiemer, S. and Wyss, M. Minimum magnitude of completeness in earthquake catalogs: Examples from Alaska, the western United States, and Japan. *Bulletin of the Seismological Society of America*, 90(4):859–869, 2000. doi: 10.1785/0119990114.

Wu, Y.-M., Chen, S.-K., Huang, T.-C., Huang, H.-H., Chao, W.-A., and Koulakov, I. Relationship between earthquake b-values and crustal

692 stresses in a young orogenic belt. *Geophysical Research Letters*, 45(4):1832–1837, 2018. doi: 10.1002/2017GL076694.

Non-peer reviewed **Research Article** submitted to SEISMICA

Supplementary Material for: The June 2026 Socorro swarm: A reactivation of rift-parallel normal faults above the Socorro Magma Body

Christopher M. Calvelage * [1], **Jessica R. Aerts** [2], **Susan L. Bilek** [2], **Urbi Basu** [2]

[1]EarthScope Consortium, Washington, D.C., USA, [2]New Mexico Institute of Mining and Technology, Socorro, New Mexico, USA

Contents This supplement provides the station geometry (Figure S1), the distribution of relative location uncertainties (Figure S2), the frequency-magnitude distributions and the sensitivity of b to the completeness magnitude (Figures S3 and S4), and per-event focal-mechanism parameters for the ten events of magnitude 3 and above (Table S1).

1 Station geometry

Figure S1 shows the full recording geometry. The three Arizona Broadband Seismic Network stations at 250 to 290 km supply the only western-azimuth first-motion polarities; the local network spans northerly and southerly azimuths only, and the eastern quadrant is unsampled because GS.NM01 and AM.R14B7 were not telemetering during the 2026 swarm.

Sixteen SmartSolo nodes were deployed over the Socorro Magma Body. Four form an eastern arm and enter the analysis as individual stations. The remaining twelve occupy a single cluster 78 m across.

2 Relative location uncertainties

Figure S2 gives the distribution of GrowClust bootstrap relative location uncertainties. The per-event resample distributions are strongly heavy-tailed, so a median-deviation statistic, which contains only half the resamples, sits at 91 m east, 32 m north and 59 m in depth, while the 95th percentile of the same distributions sits at 658 m, 315 m and 785 m.

These are relative uncertainties within similarity clusters; the absolute depth carries a larger systematic uncertainty, because of station coverage.

3 Frequency-magnitude distributions and the choice of M_c

The completeness magnitude is the most consequential parameter in the b-value comparison. Figure S3a shows b for every population as a continuous function of M_c rather than at one adopted value. The 2026 swarm lies below the

*Corresponding author: chris.calvelage@earthscope.org

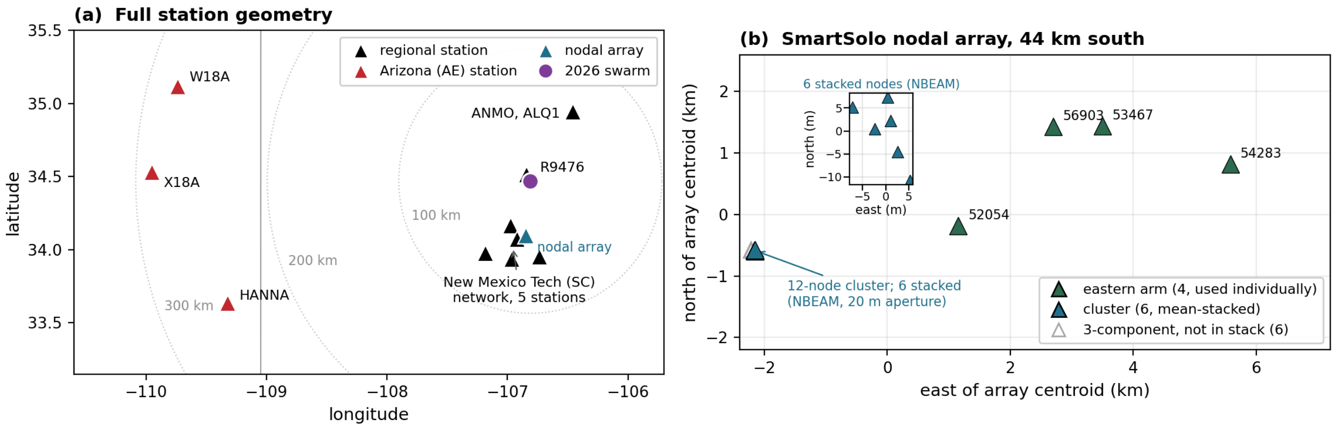

Figure S1 Station geometry. (a) All stations used, with range rings at 100, 200 and 300 km from the swarm. The Arizona (AE) stations provide the western-azimuth polarities that the local network cannot. (b) The SmartSolo nodal array in local coordinates about the array centroid, separating the four eastern-arm nodes used individually from the six vertical-component nodes that are mean-stacked into NBEAM. Open symbols are the six three-component nodes, which sit at the same cluster site but are not included in the stack. Inset: the six stacked nodes at meter scale, spanning 20 m.

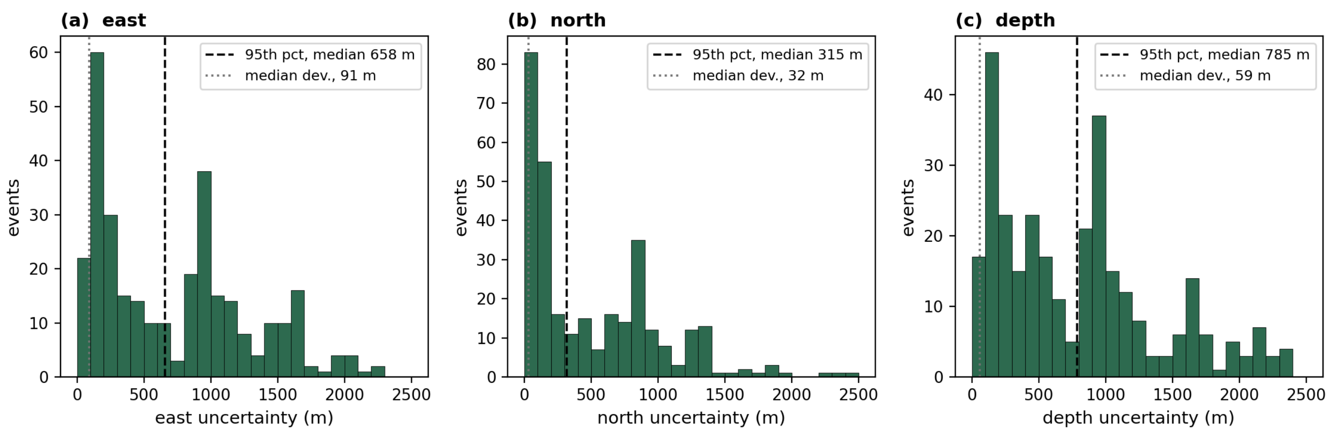

Figure S2 GrowClust bootstrap relative location uncertainties for the relocated events, in the (a) east, (b) north and (c) vertical directions. Histograms show the 95th percentile of each event's resample deviation, the quantity plotted in Figures 1 and 5 of the main text; dashed lines mark its median. Dotted lines mark the median of the median-deviation statistic for the same events, about seven times smaller, which is the measure GrowClust reports by default.

other three at every M_c examined, and the difference increases with M_c, so the adopted value of 0.4 gives a smaller contrast than any larger choice would.

Figure S3 also shows $\hat{b}$ rising steadily with M_c in every population, over the whole range and well above any plausible completeness threshold, where for a Gutenberg-Richter distribution it should be flat. The behavior is not an artifact of the magnitude alignment, since it is equally present on the native M_L scale, and not one of magnitude rounding, since the catalogs are effectively continuous in magnitude. It is instead the signature of curvature, which Figure S4 shows directly. None of the cumulative distributions are log-linear, since each falls away from its own fitted line at the large-magnitude end (panel a), and the local slope of $\log N(\geq M)$, measured in sliding 0.6-magnitude windows, is not constant anywhere (panel b). For the regional catalog it rises from near zero below -1, where the catalog is incomplete, through 0.59 at magnitude 0.5 to 1.53 near magnitude 1.7; for the 2026 swarm it rises from 0.32 to about 1.0 over the range where the swarm is well recorded. Because the Aki-Utsu estimator returns the mean local slope above whatever threshold it is given, a local slope that increases with magnitude makes $\hat{b}$ increase with M_c, roughly linearly. Figure S3a is a representation of the local slope function rather than a test of estimator stability, and the mean excess magnitude $E[M - M_c \mid M \geq M_c]$, constant for a pure exponential, falls monotonically in all four populations. No single number characterizes the b-value of these populations, and a comparison at a common M_c is not automatically a fair one. Above $M_c = 0.4$ the populations span different magnitude ranges, about 3.1 units for the 2026 swarm, 2.4 for the regional catalog and only 1.3 for the two earlier swarms. We controlled for this by refitting every population with a doubly-truncated maximum-likelihood estimator (Page, 1968) over a magnitude window that all of them share, so that each sees the same range and the same truncation. On the window $[0.4, 1.65]$ the 2026 swarm gives 0.32 (bootstrap 0.24 to 0.39) against 0.71 for 2004, 0.59 for 2012 and 0.73 for the region; on $[0.2, 1.65]$ it gives 0.18 (0.12 to 0.24) against 0.43, 0.64 and 0.58. The intervals for the 2026 swarm do not overlap those of any other population in either window, except that of the 2012 swarm on $[0.4, 1.65]$ (0.35 to 0.84), which overlaps slightly. Absolute values from a doubly-truncated fit over a narrow window are not comparable with the unbounded Aki-Utsu estimates quoted in the main text; what the control establishes is that the ordering and the approximate factor are robust (Figure S3b).

The b-positive estimator requires no completeness threshold to be chosen, but it is not independent of one, because it is designed for the transient incompleteness of aftershock sequences (van der Elst, 2021), and Lippiello and Petrillo (2024) show that it loses efficiency once events below the detection threshold are reported. Measured on our catalogs it drifts from 0.58 to 0.92 for the 2026 swarm and from 0.71 to 1.10 for the regional catalog as its own threshold $\delta_{\min}$ is raised from 0 to 1.2, agreeing with the other estimators on the ordering and giving a ratio of about 0.8 at $\delta_{\min} = 0.1$, the most conservative of the five approaches we apply.

Curvature of this kind is the shape expected when the completeness magnitude is not uniform across a catalog. Mignan (2012) shows that a constant M_c produces a distribution that is straight above a sharp corner, whereas a heterogeneous M_c produces a gradually curved one, because the catalog superposes many local exponential tails each anchored to its own threshold. Both of our populations could be heterogeneous in this sense, the regional catalog spanning two decades and the whole region above the body over which station coverage changed, and the 2026 swarm concentrating 210 of its 425 events into a single day. Splitting the regional catalog into four five-year epochs reduces the range of the local slope above the common M_c from 0.86 for the aggregate to between 0.43 and

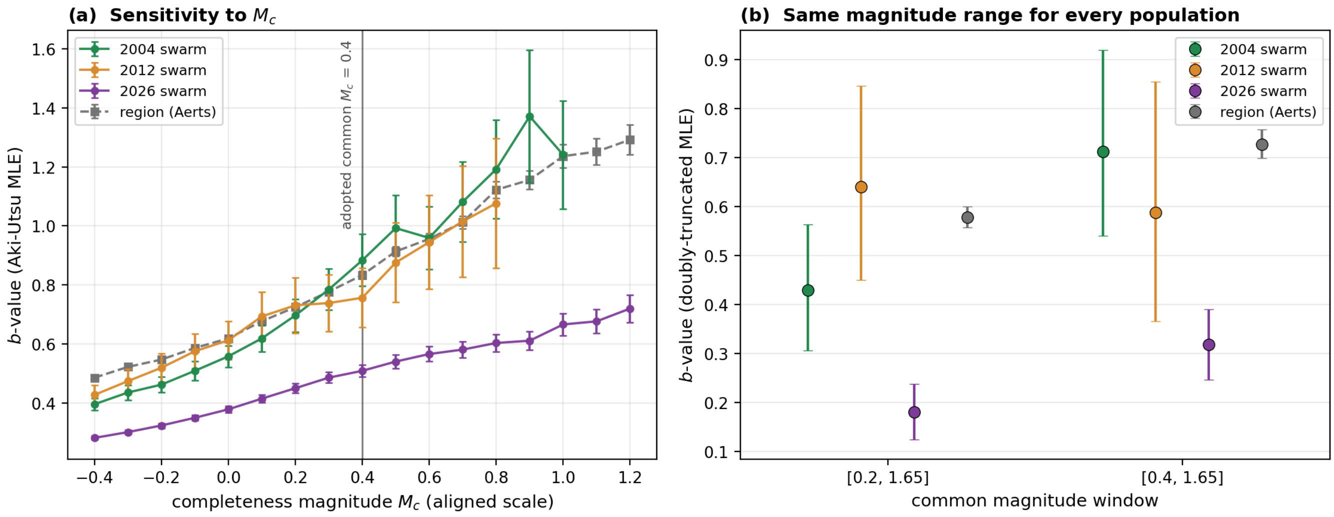

Figure S3 (a) Aki-Utsu b-value as a function of the assumed completeness magnitude, on the aligned magnitude scale, for the 2004, 2012 and 2026 swarms and the full regional catalog. Error bars are the Shi and Bolt (1982) standard error. The vertical line marks the common $M_c = 0.4$ adopted in the main text; the regional catalog is drawn dashed, as a reference population rather than a fourth swarm. $\hat{b}$ rises with M_c in every population, the signature of a lighter-than-exponential tail. (b) Control for the dynamic-range confound this creates: b refit with a doubly-truncated maximum-likelihood estimator over magnitude windows shared by all four populations, with bootstrap 16th to 84th percentile intervals. The 2026 swarm lies below the other three in both windows, and by a wider margin than at common M_c; its interval overlaps only that of the 2012 swarm on $[0.4, 1.65]$, and only slightly.

0.87 for the individual epochs, so the curvature is partly a catalog effect, but only partly, since every epoch remains strongly curved on its own. Magnitude-dependent magnitude errors may also contribute (Taroni, 2022); we have not attempted to separate the two.

Panel (c) shows the effect of treating the curvature instead as a property of the earthquakes. Fitting a tapered Gutenberg-Richter law, in which the rate rolls off above a corner magnitude, improves on a pure power law for both populations by the Akaike criterion.

The comparison in the main text remains valid, because it does not require the distributions to be Gutenberg-Richter, requiring only that the two populations be measured the same way. In every magnitude window where both are well sampled the local slope of the 2026 swarm is roughly half that of the regional catalog, 0.32 against 0.59 from 0.2 to 0.8, 0.44 against 0.87 from 0.5 to 1.1, and 0.50 against 1.08 from 0.8 to 1.4. We therefore treat the reported b-values as a comparative index measured identically across populations rather than as fitted Gutenberg-Richter slopes.

4 Focal-mechanism parameters and resolution

Table S1 lists the ten events of magnitude 3 and above for which first-motion mechanisms were attempted, with their hypocenters, the data available for each, and the effect of adding the western Arizona polarities. Adding those polarities shrinks the acceptable-mechanism set by 56 percent on average and closes the azimuthal gap for five of the ten events, but the acceptable sets remain large, so no individual small-event mechanism is well resolved and we rely on the regional moment tensor of the largest event for the definitive normal mechanism.

The three events with a preferred strike-slip solution cover nearly the whole depth and map extent of the group rather than forming a distinct sub-volume, spanning 9.0 to 12.3 km in depth against 8.2 to 12.9 km for the full set, and their acceptable clouds overlap normal-faulting orientations (Figure 6 of the main text).

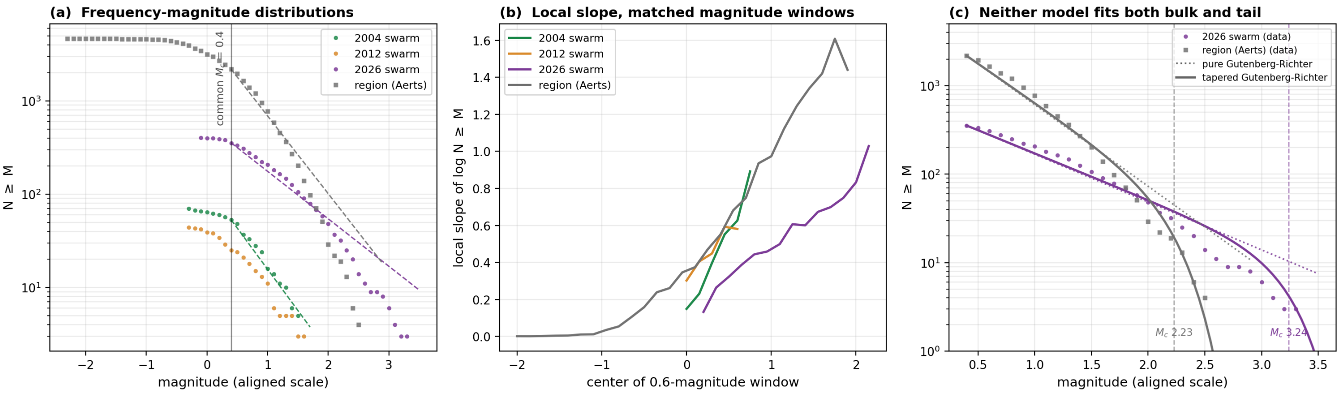

Figure S4 Frequency-magnitude distributions of the four populations on the aligned magnitude scale. (a) Cumulative distributions, with each population's Aki-Utsu fit at the common M_c of 0.4 shown dashed. Every distribution bends below its own fitted line at large magnitude, so none is log-linear. The vertical line marks the common M_c. (b) Local slope of $\log N(\geq M)$ in sliding 0.6-magnitude windows, which for a Gutenberg-Richter distribution would be a horizontal line at b. The slope increases with magnitude in every population, and the 2026 swarm lies below the regional catalog throughout the range where both are sampled. The steep fall in the regional curve below magnitude -1 is the detection rollover, not a property of the earthquakes. (c) Pure and tapered Gutenberg-Richter fits to the 2026 swarm and the regional catalog, with the Akaike information criterion for each; the tapered model fits the bulk better but assigns negligible probability to the largest observed events, so we do not interpret its corner magnitude.

Table S1 Focal-mechanism parameters and resolution for the ten events of magnitude 3 and above. Hypocenters are from the GrowClust catalog; M is the USGS network magnitude (U.S. Geological Survey, 2017) and M_L the local magnitude of this study. N_{pol} is the number of local first-motion polarities and $N_{S/P}$ the number of S/P amplitude ratios. The paired columns give the value using local stations only and then after adding the western Arizona polarities: azimuthal gap, size of the acceptable-mechanism set, and the P/T axis scatter of that set. The preferred style is that of the west-augmented solution shown in Figure 6 of the main text.

Ev	Origin time (UTC)	Lat. (deg)	Lon. (deg)	Depth (km)	M USGS	M_L this study	N_{pol}	$N_{S/P}$	Gap (deg) loc./+W	Acceptable loc./+W	Scatter (deg) loc./+W	Preferred style
1	2026-06-14 02:33:39	34.4883	-106.8856	9.9	3.2	3.28	8	4	192 / 150	3018 / 1750	19.3 / 19.3	normal
2	2026-06-14 17:38:09	34.4622	-106.7999	10.9	3.7	3.34	8	4	144 / 144	2346 / 585	17.3 / 13.0	normal
3	2026-06-14 17:41:00	34.4700	-106.7555	10.0	3.9	3.90	8	6	151 / 151	2331 / 186	20.6 / 14.3	normal
4	2026-06-17 09:44:33	34.4617	-106.7648	12.3	3.3	3.01	6	3	149 / 149	3846 / 2924	20.1 / 19.8	strike-slip
5	2026-06-17 10:25:34	34.4277	-106.7178	12.9	3.1	3.18	8	4	156 / 156	2937 / 320	20.1 / 17.0	normal
6	2026-06-17 10:46:31	34.5609	-106.8520	10.1	3.8	3.52	8	5	196 / 127	2673 / 366	19.5 / 17.0	normal
7	2026-06-17 12:44:13	34.4801	-106.8586	8.2	3.5	3.37	8	4	181 / 133	1016 / 1071	21.4 / 19.8	normal
8	2026-06-17 13:15:31	34.5095	-106.8719	9.0	3.2	3.27	8	4	194 / 151	697 / 303	20.2 / 20.2	strike-slip
9	2026-06-17 17:14:06	34.4880	-106.8062	9.3	3.7	3.88	8	5	141 / 141	949 / 662	22.5 / 21.2	strike-slip
10	2026-06-17 18:56:56	34.4773	-106.8657	10.1	3.8	3.67	8	3	190 / 129	2116 / 570	18.3 / 16.1	normal

References

Lippiello, E. and Petrillo, G. b-more-incomplete and b-more-positive: Insights on a robust estimator of magnitude distribution. *Journal of Geophysical Research: Solid Earth*, 129(2):e2023JB027849, 2024. doi: 10.1029/2023JB027849.

Mignan, A. Functional shape of the earthquake frequency-magnitude distribution and completeness magnitude. *Journal of Geophysical Research: Solid Earth*, 117(B8):B08302, 2012. doi: 10.1029/2012JB009347.

Page, R. Aftershocks and microaftershocks of the great Alaska earthquake of 1964. *Bulletin of the Seismological Society of America*, 58(3): 1131–1168, 1968.

Shi, Y. and Bolt, B. A. The standard error of the magnitude-frequency b value. *Bulletin of the Seismological Society of America*, 72(5):1677–1687, 1982. doi: 10.1785/BSSA0720051677.

Taroni, M. The effect of magnitude uncertainty on the Gutenberg–Richter b-value estimation and the magnitude–frequency distribution: 'What hump?'. *Geophysical Journal International*, 231(2):907–911, 2022. doi: 10.1093/gji/ggac219.

U.S. Geological Survey. Advanced National Seismic System (ANSS) Comprehensive Catalog [Data set], 2017. doi: 10.5066/F7MS3QZH.

van der Elst, N. J. *B*-positive: A robust estimator of aftershock magnitude distribution in transiently incomplete catalogs. *Journal of Geophysical Research: Solid Earth*, 126(2):e2020JB021027, 2021. doi: 10.1029/2020JB021027.